Structural and Functional Biomedical Imaging Using Polarization-Based Optical Coherence Tomography

A DISSERTATION

SUBMITTED TO THE FACULTY OF THE GRADUATE SCHOOL

OF THE UNIVERSITY OF MINNESOTA

BY

ADAM J BLACK

IN PARTIAL FULFILLMENT OF THE REQUIREMENTS

FOR THE DEGREE OF

DOCTOR OF PHILOSOPHY

Adviser: Taner Akkin

August, 2015

August, 2015

Acknowledgements

I would like to thank my adviser, Dr. Taner Akkin, for his help and guidance throughout my graduate program. I entered the lab without much optics experience and he spent many long hours with me in the lab building and testing systems from square one. His passion for the research and creativity in the lab and analysis helped me approach roadblocks in my research in new ways and overcome obstacles to ultimately find a solution or redefine problems.

Dr. Robert Miller and his lab have been very helpful in their guidance for preparing and recording from retina samples. With the help of Steve Sullivan and Eric Gustafson I was able to perform all aspects of the dissection and perfusion to obtain viable samples for my research. I would also like to thank Dr. Theoden Netoff and his lab for their support in electrode preparations, especially from Vivek Nagaraj. I would like to acknowledge and thank Dr. Shai Ashkenazi for serving on my committee throughout my graduate program. Dr. Alena Talkachova and Rebecca Smith were instrumental in their help with cardiac imaging. From technical discussions to sample preparations and experimental design their expertise and assistance continued to be useful resulting in a fruitful collaboration.

I would like to thank lab members Muhammad Al-Qaisi and Hui Wang for their instruction since I started in the lab and throughout their time at the university. Tina Yeh, Hui Wang and her husband Junfeng made out summer at MBL most enjoyable. I am grateful for all the useful discussions from my fellow lab members Hui, Tina, and Chao Liu.

I cannot thank my family, especially my wife Katie enough for their encouragement, support and understanding. All the major life events we've been through during my time at the university has brought me the greatest joys of my life; our two sons Sebastian and Dashielle.

Abstract

Biomedical imaging has had an enormous impact in medicine and research. There are numerous imaging modalities covering a large range of spatial and temporal scales, penetration depths, along with indicators for function and disease. As these imaging technologies mature, the quality of the images they produce increases to resolve finer details with greater contrast at higher speeds which aids in a faster, more accurate diagnosis in the clinic. In this dissertation, polarization-based optical coherence tomography (OCT) systems are used and developed to image biological structure and function with greater speeds, signal-to-noise (SNR) and stability. OCT can image with spatial and temporal resolutions in the micro range. When imaging any sample, feedback is very important to verify the fidelity and desired location on the sample being imaged. To increase frame rates for display as well as data throughput, field-programmable gate arrays (FPGAs) were used with custom algorithms to realize real-time display and streaming output for continuous acquisition of large datasets of swept-source OCT systems. For spectral domain (SD) OCT systems, significant increases in signal-to-noise ratios were achieved from a custom balanced detection (BD) OCT system. The BD system doubled measured signals while reducing common term. For functional imaging, a real-time directed scanner was introduced to visualize the 3D image of a sample to identify regions of interest prior to recording. Elucidating the characteristics of functional OCT signals with the aid of simulations, novel processing methods were also developed to stabilize samples being imaged and identify possible origins of functional signals being measured. Polarization-sensitive OCT was used to image cardiac tissue before and after clearing to identify the regions of vascular perfusion from a coronary artery. The resulting 3D

image provides a visualization of the perfusion boundaries for the tissue that would be damaged from a myocardial infarction to possibly identity features that lead to fatal cardiac arrhythmias. 3D functional imaging was used to measure functional retinal activity from a light stimulus. In some cases, single trial responses were possible; measured at the outer segment of the photoreceptor layer. The morphology and time-course of these signals are similar to the intrinsic optical signals reported from phototransduction. Assessing function in the retina could aid in early detection of degenerative diseases of the retina, such as glaucoma and macular degeneration.

Table of Contents

List of Figures

Chapter 1

Introduction

1.1 Overview

Investigating biological samples with light has elucidated function and resolved the microscopic world. Optical properties of tissues are exploited as they are discovered that help guide other fields of research. With both intensity and polarization information available, various properties of tissue can be probed simultaneously. Changes in optical properties of samples, such as scattered light and birefringence, offer measures of structure, orientation and activity. In this work I used polarization-based optical coherence tomography (OCT) to image biological tissues to measure structure and function using custom developed high-performance, high-precision hardware and software.

OCT is an established imaging technology for measuring micro-scale structures in biological tissue. The maturity of OCT, with its many variants, speed and SNR capabilities, have investigated a variety of biological structures and even function. The capabilities and limitations of OCT and its variants are well characterized and confirmed with feasibility studies demonstrating repeatable signals for functionally imaging squid giant axon action potentials, neural activity from brain slices and retina activation from a light stimulus from several animal models, including humans [1-6]. These results with many others have quickly established OCT as an imaging technology that has unique utility in the clinic with its noninvasive nature, ability to resolve fine detail and depth penetration in tissue. OCT is equipped to extend its reach to examine

more basic science questions with its unique imaging scales and characteristics. In this dissertation, I will describe our work for increasing OCT performance for Fourier domain OCT systems, development of a balanced detection spectral domain OCT system and imaging the heart and retina to elucidate structure and function with high resolution.

1.2 Motivations for Research

An important aspect of diagnostic tools used in research and the clinic is a thorough evaluation of a sample with a stress on early detection; this includes both structural and functional characteristics. By the time many diseases express themselves structurally, the efficacy of any treatment is greatly impacted depending on how far the disease has progressed. Depth-resolved imaging has been suggested as a powerful technique with great potential for *in vivo* diagnostics that can provide information about biological tissue from many different perspectives (functional or chemically specific information) [7]. OCT has commonly been referred to as providing an "optical biopsy" for a variety of tissues and locations, including endoscopy [8-10]. The unique characteristics of OCT, being depth-resolved, high speed, high resolution and noninvasive, position it well to take an early diagnostic role in not only identifying but understanding certain pathologies.

An obstacle in producing a clinical-grade device for OCT is the ability to get instant feedback on structural and functional information. This feature requires high-performance hardware and software. In the world of big data, visualizing large datasets and storing them is becoming a limiting factor. This can be addressed with smart, efficient algorithms to acquire, process, and visualize large datasets with high throughput.

1.3 Organization of this dissertation

Chapter 2 discusses the background and principles of OCT. The parameters that define an OCT system and how performance is measured will be covered. Common OCT implementations will also be discussed with a focus on the systems configurations that are the basis for imaging setups used in this work.

Chapter 3 will describe advancements in real-time OCT processing for FPGA-based real-time algorithms to achieve high data throughput rates and accurate k-space remapping during acquisition. These advancements were applied without sacrificing the size or quality of the images acquired and reach the limit for continuous streaming and storing of data with commercially available hardware. The addition of complete system synchronization for functional 3D imaging using a directed scanner is also discussed.

Chapter 4 presents a balanced detection spectral-domain OCT system. Using only one set of detection optics with an area camera, two modulated spectra are produced that are completely out of phase and subtracted to double the measured signal. Common noise terms that are present on both spectra are therefore removed, improving image quality. This system also maintains signal gains in depth which, with the higher SNR, could increase the available depth for imaging.

Chapter 5 looks at an application of polarization-sensitive OCT for measuring the geometry of the perfusion boundary in a rabbit heart. Isolated rabbit hearts were imaged before and after clearing and a clear delineation between perfused and nonperfused tissue can be observed, which are shown to be complex interdigitated "fingers".

Chapter 6 uses the developed directed scanner to image structure and function of the salamander retina. Eyecup preparations are stimulated with white light while 3D volumes are acquired using OCT. Several processing methods are demonstrated to stabilize the sample and characterize the signals measured and how they relate to their physiologic origin.

Chapter 7 will conclude the dissertation with an outlook for high-performance polarization-based imaging and the applications to imaging cardiac and retinal tissues.

Chapter 2

Optical Coherence Tomography

2.1 Overview

Optical coherence tomography (OCT) is a low-coherent interferometric technique for imaging optically scattering media, such as biological tissue. OCT typically uses near-infrared light (NIR) to penetrate tissue up to a few millimeters while not being largely absorbed by water; taking advantage of the depth-resolved nature of OCT. The spatial resolution is in the micrometer range and fast temporal resolutions (kHz to GHz per scan) are possible. OCT fills a gap in imaging scales between confocal microscopy and ultrasound having greater spatial and temporal resolution than ultrasound but shallower penetration depth. The depth penetration of OCT is, however, greater than confocal microscopy while the spatial resolutions are comparable yet confocal microscopy is capable of resolving finer detail (< 1 μm). However, high NA microscope objectives or adaptive optics approaches can be implemented for optical coherence microscopy (OCM). OCT is a depth-resolved technique, allowing for repeatedly imaging sample volumes without changing focus of the sample optics or position of the sample. The spatial and lateral resolution of OCT systems are independent of one another allowing changes in depth resolutions or lateral directions without one directly affecting the resolution of the other. OCT is also noninvasive; penetration of an imaging beam is dependent on the sample being imaged but in general is in the millimeter range. This limitation can require deeper tissues to be exposed for imaging or accessed via an endoscope. When imaging the retina, OCT is an attractive method

since the retina is weakly scattering, noninvasive access is possible through the cornea and it can be sufficiently imaged with a power low enough to comply with ANSI safety standards. OCT has also been used for functional studies which have additional benefits since light does not couple into electrical stimulus or recording which reduces possible artifacts for recording neural activity. The signals measured with OCT are capable of providing several contrasts from small nano-motions, scattering/absorption changes, retardance, relative optical-axis orientation and Doppler flow. With scanning, 4D imaging is possible with micro-scale spatial resolution and millisecond temporal resolution which will be demonstrated.

2.2 Theory

OCT was first described in 1991 [11] for imaging biological tissue, primarily the retina and arteries, which remain the primary applications of the technology today. The configuration for the seminal work is known as a time-domain (TD) system. Since then, OCT has since generated much interest into research, specialized applications and improvements of the technology. Innovations in OCT in past decades have resulted in a variety of system configurations, each with their benefits and drawbacks, some of which are discussed herein. A Typical OCT system is based on a Michelson interferometer, composed of a source, sample, reference and detection arm shown in Fig 2.1. The optical path difference between the reference and sample arm must be within a coherence length for interference to occur. The field from the reference, E_r, and the sample, E_s, interfere with delay τ and the power measured on a detector (I_d) result in

$$\boldsymbol{I_d = \langle |E_r(t)E_s^*(t+\tau)|^2 \rangle = 0.5 * (I_r + I_s) + |G(\tau)| \cos[2\pi\nu_o\tau + \phi(\tau)]} \qquad \textbf{2.1}$$

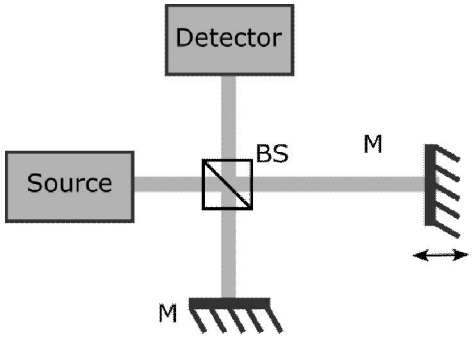

Figure 2.1. Schematic of Michelson interferometer. BS, beamsplitter; M, mirror. The double sided arrow represents the mirror that moves to produce interference.

where $|G(\tau)|$ is the temporal coherence function with argument $\varphi(\tau)$. I_r and I_s are the DC intensities that carry no depth information and v_o is the center optical frequency of the source where $v_o = c/\lambda_o$ with c being the speed of light and λ_o is the center wavelength of the source. The depth profile (A-Scan or A-Line) for TD systems is acquired in time, since it is photodetector based, by moving the reference mirror to change the depth location for interference to occur. For SD systems, on the other hand, the spectrum is acquired from a spectrometer, typically consisting of a grating and line scan camera, and the independent variable is the wavenumber, k. The reference and sample field are now given respectively as $E_r e^{i2kz_r}$ and $E_s e^{i2kz_{sn}}$ where z_r is the distance from the reference arm and z_{sn} the distance from a discrete sample reflector. The interference resulting for each k is then

$$I_d(k) = S(k)R_rR_{sn} + S(k)\sum_{n=1}^{N}\sqrt{R_rR_{s_n}}\left(\cos\left[2k\left(z_r - z_{s_n}\right)\right]\right) \; +$$

$$S(k)\sum_{n\neq m=1}^{N}\sqrt{R_rR_{sn}}\left(\cos\left[2k\left(z_{s_n} - z_{s_m}\right)\right]\right) \qquad \textbf{2.2}$$

where the three components being added are the DC term, cross correlation terms (sample interfering with reference; desired signal), and auto-interference (sample interfering with itself) respectively. It is important to note the relation between TD and SD methods. The Wiener-Khintchen theorem describes the relation between the temporal coherence function and the power spectral density via the Fourier transform

$$G(\tau) = FT^{-1}\{S(v)\} \qquad \textbf{2.3}$$

This property allows SD systems to acquire an entire A-Line in a single shot without moving the reference arm. Removal of the mechanical scanning requirement increases the system's sensitivity and stability [12]. One disadvantage that results from this method is the auto-interference terms. This can be reduced, however, by increasing the reference power to reduce their visibility with respect to the interference signal since the auto-interference power contribution is linear.

2.3 System Parameters

2.3.1 Resolution

Since OCT is based on low-coherence interferometry, the larger the bandwidth of the source, the smaller the coherence length. The coherence length of a source, which determines the axial resolution of an OCT system, is based on its center wavelength and bandwidth. The equation for the coherence length is

$$\boldsymbol{l_c = \frac{2\ln(2)}{\pi}\frac{\lambda_o^2}{\Delta\lambda}} \qquad \textbf{2.4}$$

with λ_o being the center wavelength of the source and $\Delta\lambda$ the source bandwidth (full width at half maxima). The lateral resolution is determined by the sample arm optics. There is a tradeoff between lateral resolution and depth of field for focusing as seen in Fig 2.2. The tighter the focus, the less light will be backscattered in depths not within the Raleigh range. The Raleigh range is related to the beam waist by the following equation

$$\boldsymbol{Z_R = \frac{\pi\omega_o^2}{\lambda}} \qquad \textbf{2.5}$$

where Z_R is the Rayleigh length, ω_o is the beam waist and λ is the center wavelength. A scan lens is typically used to maintain a flat focal plane. The lateral resolution can be made complementary to axial resolution. If a microscope objective (10-20x) is used, lateral resolution can be improved to a few micrometers.

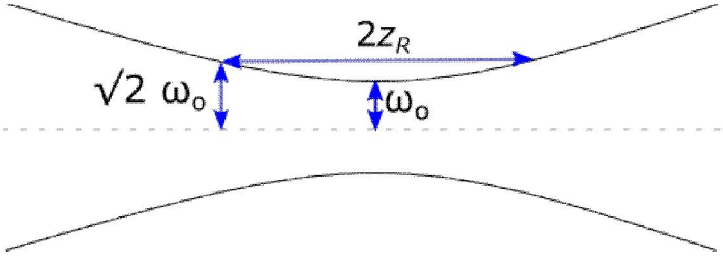

Figure 2.2. Diagram of beam waist and the Raleigh range and how they relate to the shape of the beam. Z_R, Rayleigh length; ω_o, beam waist.

2.3.2 Sensitivity, Stability & Decay

The ability to detect weak reflectors in a sample is an important property of OCT that makes it beneficial to imaging nearly translucent samples. The sensitivity of an OCT system depends on noise sources (read out and dark noise, shot noise and relative intensity noise, RIN) and the power of light returning from the reference and sample arm. SNR is optimized when shot noise dominates the other noise sources [13] with optimum reference power (equal to RIN and receiver noise) [14]. The two components comprising the sensitivity are the attenuation and SNR. The attenuation is measured by recording the power in the detection arm after placing a mirror as a sample to return maximum light to the detection arm. Next the sample light is attenuated until the coherence function peak from the mirror is no longer saturating and the power at the detection arm is measured again. The ratio of these two power levels is the attenuation. To experimentally obtain the SNR, the ratio of the peak of a coherence function to the average power of the noise level in the imaging range is calculated. The sum of the attenuation and SNR is the system's sensitivity. Fourier domain OCT systems demonstrate greater sensitivity (~100 dB) than TD systems upwards of 30 dB [15] which are more prominent with faster integration times [16] due to the phase fluctuations during acquisition that affect phase stability and signal magnitude. The

reduction of coherence function amplitude during the integration time can be further degraded by motion artifacts which is called fringe washout. Faster integration times will reduce fringe washout but at some point RIN noise starts to impact SNR. One way to reduce this effect is implementing a balanced detection system, the focus of Chapter 4.

Small perturbations in the optical path difference between reflectors can be observed by the phase component of the complex depth profile in SD OCT and indicates the noise level for which functional signals can be measured. The phase stability of a system can be affected by environmental perturbations, system noise, small mechanical vibrations (motion artifacts) and the magnitude of the signals and noise levels (SNR). Phase stability is characterized by measuring the phase signal from a single auto-interference peak. Typically, this is accomplished by using a coverslip; the front and back surface of the coverslip interfere producing an auto-interference peak where its depth position in the resulting image is equal to the optical thickness of the coverslip (the refractive index of coverslip would need to be used to obtain physical thickness). The standard deviation of the auto-interference peak from consecutive A-Line recordings results in the phase stability in radians. The optical path is double-pass and so converting from radians to meters is accomplished by

$$\boldsymbol{\phi = \lambda_o \frac{\Delta p}{4\pi}} \qquad \textbf{2.6}$$

Typical ranges for this measurement are between less than a hundred picometers to a nanometer. Swelling, optical thickness changes and other small mechanical motions of a sample that are indicators of function can be consistently measured using the phase signal. Determining the phenomena responsible for the observed changes will be discussed in Chapter 6.

One disadvantage of SD OCT is the signal decay in depth that is a result of sampling of the spectral modulations on a rectangular-pixel camera and the resolution of the spectrometer. The FWHM of the spectral resolution (smallest bandwidth the spectrometer can resolve) and the rectangular pixel shape are convolved in the k-domain which corresponds to a multiplication in the depth domain represents by the following equation for sensitivity reduction [14],

$$\boldsymbol{R(z) = \frac{sin^2(\pi z/2d)}{(\pi z/2d)^2} exp\left[-\frac{\pi^2\omega^2}{8\ln 2}\left(\frac{z}{d}\right)^2\right]} \qquad \mathbf{2.7}$$

d is the maximum depth (Nyquist limit) that can be measured and ω is the ratio of the spectral resolution to the sampling interval.

2.4 From Interferogram to Image

After acquiring an OCT depth profile with an SD OCT system, the spectral modulations are linear in wavelength. The Fourier dual to depth is wavenumber ($k = 2\pi/\lambda$), so the acquired spectra needs to be resampled to k-space. Several calibration methods have been used with good results. A grating equation can be helpful initially if all the parameters are tightly controlled but empirical measurements yield the best results due to small imperfections and misalignments in the optics. Using a calibrated commercial spectrometer and monochromater is accurate and easy to implement; a diagram is given in Fig. 2.3. After interpolation to linear k-space, dispersion mismatch between the sample and reference arms of the system can be compensated with software methods to produce coherence functions with a coherence length approaching the theoretical value. Alternately, dispersion can be balanced by hardware methods by using similar

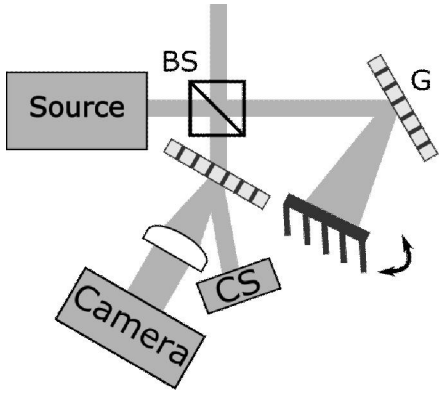

Figure 2.3. Schematic of monochronometer used for wavelength mapping. BS, beamsplitter; G, grating; CS, commercial spectrometer

components in the reference and sample arms. Each wavelength may have a different path length through the optical elements resulting in more frequencies present in the spectrum, which widens the coherence function. Adjusting all the phase values to zero for each frequency component of the coherence function results in a narrower, dispersion-compensated coherence function. This is accomplished by first taking a single reflector as a sample to obtain one coherence function and center it around zero. This maintains symmetry for the inverse Fourier transform of the coherence function. The phase of the frequency components are all corrected to zero and each acquired spectra are multiplied by the calculated phase correction (complex exponential) to shift the components accordingly. This process is a consequence of the Fourier transform; the addition of frequencies of the same phase approach a Dirac delta function. An example of coherence functions before and after dispersion compensation are shown below in Fig. 2.4. To display a final image, the base 10 logarithm of the absolute value of the complex depth profile is applied. This is the conventional OCT signal, reflectivity. In the case of PS systems, the two channels are added together to obtain the reflectivity.

Due to the interferometric nature of OCT, fixed pattern lines on an image are a common occurrence. They can be removed by recording an image with only the reference path. With the sample arm blocked, only fixed lines remain with no signal. The recorded background is then averaged in time and subtracted from future A-Lines. In some cases, median subtraction of a cross section will remove fixed pattern lines without affecting the image a great deal.

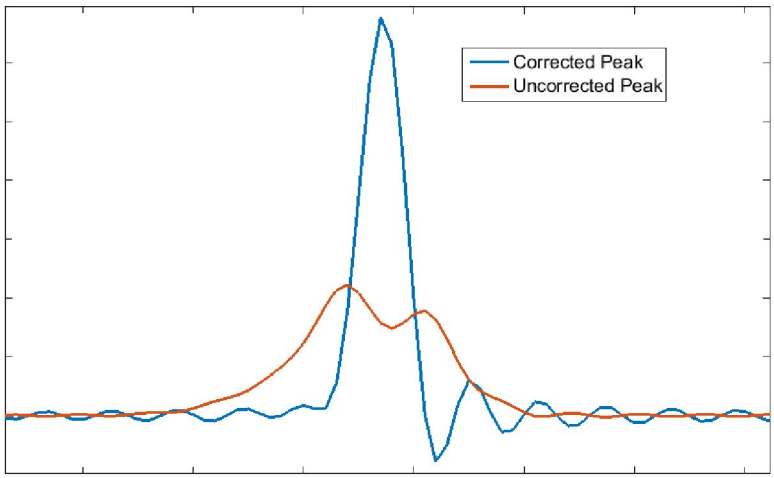

Figure 2.4. Coherence function before and after dispersion compensation.

2.6 Polarization Sensitive OCT

Initially OCT was based off an all-bulk system. With the increased availability of optical fiber due to the communication industry, high performance fiber is available at lower cost. Greater flexibility can be obtained in an OCT system by using single-mode fiber. For polarization-sensitive configurations, polarization-maintaining fiber (PMF) can be used. A diagram of a PMF cross section is shown in Fig. 2.5. The core of the fiber contains the coupled light and the two

rods affects the stress on the core resulting in a refractive index difference between the orthogonal directions. Therefore, PMF is birefringent, has fast and slow channels and maintains the polarization propagating in these channels. As will be seen in Chapter 4, PMF can be used in non polarization-sensitive systems to encode light from the reference and sample arm into orthogonal polarization states to realize balanced detection SD OCT.

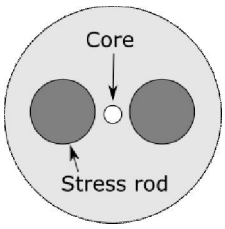

Figure 2.5. Diagram of polarization-maintaining fiber.

For PS SD OCT systems, the incident light on the sample is coupled into only one channel and prior to illuminating the sample, is made circularly polarized with a quarter-wave plate (QWP) oriented at 45°. The QWP shifts the phase of the incident light between the orthogonal polarization states, thereby changing the state; which is represented with Jones calculus. Light returning from the sample arm is coupled into the opposite channel if the sample is not birefringent (i.e. fast channel returns and couples to slow). If the sample is birefringent, there will be sample light present on both channels. Light from the reference arm is launched into both channels equally (i.e. slow channels return and couple equally to fast and slow channels). This is accomplished by a QWP with axis oriented at 22.5° to the incoming reference light. Jones calculus is a mathematical description of polarized light. The incident light is referred to as the Jones vector and represents the orthogonal polarized states as

$$\begin{pmatrix} E_x \\ E_y \end{pmatrix} \qquad \textbf{2.8}$$

The difference of phase retardance between the fast and slow axis, ϕ, with an orientation of fast axis to the horizontal axis given by θ, the transformation matrix is given as

$$\begin{pmatrix} \mathbf{e^{i\phi/2}\cos^2\theta + e^{-i\phi/2}\sin^2\theta} & \mathbf{(e^{i\phi/2} - e^{i\phi/2})\cos\theta\sin\theta} \\ \mathbf{(e^{i\phi/2} - e^{-i\phi/2})\cos\theta\sin\theta} & \mathbf{e^{i\phi/2}\sin^2\theta + e^{-i\phi/2}\cos^2\theta} \end{pmatrix} \quad \textbf{2.9}$$

To obtain the resulting Jones vector, the Jones matrix is multiplied by the Jones vector. In PS OCT, the reference arm launches light from one channel of PMF and couples back into both channel equally by placing a QWP at 22.5° to the fast axis. The sample arm QWP is oriented at 45° to flip the launched light from one channel to the other. PS OCT systems have a more complete representation of the sample since circularly polarized light is launched on the sample and both channels are coupled back into the system to interfere with the reference. This provides PS OCT systems with two additional contrasts, retardance and optical axis orientation. Let A_1 and A_2 represent the two polarization channels in a PS system, then the standard reflectivity (R), retardance (δ) and optical axis orientation (θ) at depth z is given by [17]

$$\boldsymbol{R(z) \propto A_1(z)^2 + A_2(z)^2} \quad \textbf{2.10}$$

$$\boldsymbol{\delta(z) = \tan^{-1}\left(\frac{A_1(z)}{A_2(z)}\right)} \qquad \boldsymbol{\theta(z) = \frac{\pi - (\Phi_1(z) - \Phi_2(z))}{2}} \quad \textbf{2.11}$$

where Φ_n is the phase of the complex depth profile for its respective channel n. Because of a time-varying phase offset, $\theta(t)$ indicates a relative measurement for the PMF system.

2.5 Fourier Domain System Implementations

SD OCT systems encode the depth profile as modulations of the source spectrum via a calibrated spectrometer [18]. This reduces the need for scanning the reference mirror and allows SD OCT to have a much greater sensitivity [12]. The spectrometer is an important part of an SD system. The resolution of the spectrometer along with the wavelength resolution of the camera can determine signal decay in depth which can degrade the quality of an SD OCT system if the components are not chosen properly. For PS operations, the polarization states need to be split at the spectrometer. This can be accomplished with a Wollaston prism, which separates orthogonal polarization states at a pre-determined angle. This is typically done horizontally, using half of the cameras pixels for each channel, which allows operation with a single camera. Splitting the spectra can also be done vertically using a dual line or area camera.

Swept source (SS) OCT is another Fourier domain OCT technique that doesn't use a spectrometer with a line scan camera, but is photo-receiver based. One advantage of having a photo-receiver based system is that balanced detection can be easily implemented yielding high SNR compared to other systems. The swept source operates by encoding the spectrum in time. This is done with a sweeping laser or a monochronometer that can utilize a rotating polygon mirror as a spectral filter. Swept sources can exceed scan rates of 100 kHz.

With the introduction of Fourier domain methods, faster acquisition rates and increased sensitivity have been demonstrated compared to time-domain setups [12, 15, 16]. As scan rates increase to improve image stability and the fidelity of functional biomedical imaging, increasing the SNR has become a subject of OCT research. Dominant noise sources in OCT imaging can

originate from the light source, interferometers and detectors. Since OCT's introduction, many specializations and new techniques continue to broaden the applicable areas and situations for OCT to operate and develop. Most new implementations of OCT aim to increase resolution, speed, and/or SNR. Increases of the latter rely on stable sources, fast and shot-noise-limited acquisition. More recently, with faster imaging speeds, OCT has been used for functional studies. These types of measurements require fast, stable acquisition that must be tightly synchronized from stimulus to detection. Real-time processing is also necessary to ensure the fidelity and real-time use of signals being measured. In the next couple of chapters, a new system design for balanced detection for SD OCT systems is demonstrated and high-speed real-time acquisition and storage for a PS SS OCT system is implemented.

Chapter 3

High-Speed Real-Time Data Acquisition and Display

3.1 Overview

Achieving a greater image quality with OCT requires a greater sensitivity and decreased integration times to reduce fringe washout. Obtaining a faster A-Line acquisition rate also requires an increase in data throughput and processing power. Using field-programmable gate arrays (FPGAs), the acquisition process can be pipelined, which works like an assembly line. The amount of logic processing that is possible in each clock tick is dependent on the propagation delay of each logic component through the electronic gates. This results in high performance by maximizing the amount of computation done within each clock cycle. Data can be acquired with sampling rates of 250 MS/s and higher with a high throughput around 5.6 GS/s with newer hardware capable of greater throughput continues to become developed. With high-resolution high-speed systems, considerable processing and storage are required as well as maintaining a real-time display of the sample. In this chapter, I will discuss high-performance methods for real-time processing for SS OCT images and capabilities for high-speed, high-throughput, real-time acquisition and its comparison to other architectures. To accomplish this, we realized a method for real-time resampling for a functional PS SS OCT systems that can handle fast A-lines and continuous saving that is limited only by the computer system's RAM and hard drive configuration. The system is also synchronized to the clock cycle across acquisition, processing

and control while capable of handling multiple galvanometer scanning mirrors, analog/digital stimulus/triggering and recording channels.

3.2 Introduction

Improvements in high-speed scanning for TD OCT systems allowed for real-time imaging for small scans (300-400 A-Lines) at rates of 4-8 frames per second [19, 20] using conventional CPU processing methods. With the introduction of SD OCT, the requirement of scanning for each depth profile was no longer a limiting factor and data throughput and optimized software implementations of image calculations as well as image display became the bottleneck. Producing a high-fidelity real-time OCT image can be computationally expensive and there has been effort to reduce the amount of time taken for these operations. Early optimizations of real-time processing [21, 22] including FPGAs and digital signal processors (DSP) have made significant progress establishing a framework for real-time OCT signal processing. More recently, real-time processing has been receiving greater attention [23, 24] to keep up with advancements in acquisition hardware which has reached sampling speeds of 250 MHz and higher for up to four channels. In PS SS OCT systems, four channels would include two polarization channels that carry image information from the sample, one k-clock channel and a trigger channel to indicate the acquisition of a spectrum. With the addition of polarization-sensitive systems, the amount of computation required for each A-line increases [25]. While several groups have reported very fast systems from 300-500 kHz [26, 27] to even multi-megahertz [28], the number of points in a scan is compromised to achieve these rates which limits imaging depth and sensitivity decay. In this

system, the OCT system sampling rate is increased to the maximum rate allowed while still being able to stream data continuously withouth compromising the number of scan points.

There are a variety of FPGA implementations for real-time OCT processing but the major components are acquisition, processing and transmission to the host. To increase performance, interpolation is also calculated on the FPGA. First, the data are acquired; acquisition methods are different from SS to SD but once the spectra are acquired, processing is very similar to produce the depth profiles. SD systems typically use the camera link interface for high-speed operations and un-packaging of data are accomplished by configuring the acquisition code to the specific camera's tap geometry setting. The tap geometry specifies how many pixels are transmitted per clock cycle on the four available cameral link ports and at what bit depth (e.g. 2-tap-12 or 4-tap-8 for a line scan camera). The standard clock of the camera link interface is 40 or 80 MHz which limits the throughput (while maintaining full A-Line length and bit depth) for a 2048 pixel camera to ~100 kHz. For SS acquisition, the interference fringes are sampled directly in time and no further packaging is required. If the maximum sampling rate possible for a given hardware configuration is not required for a specific sample or method, an average can be used to reduce the noise of each sample. Our FPGA implementation can sample up to 250 MHz and has been used with a signal averaging of 5 samples resulting in a 50 MHz sampling rate which is proper for our home-built swept-source yields a scan rate of 48 kHz. FPGA programming is usually done in low-level languages such as VHDL and Verilog. LabVIEW has an FPGA module using Xilinx FPGAs and component-level intellectual property (CLIP) that reduces design time, makes complex algorithm design possible and increases the accessibility of FPGA-based systems, opening it up to a wider audience.

3.3 FPGA Implementation

In FPGA programming, operations are pipelined which works like an assembly line. The amount of time between each operational block is determined by the clock speed of the loop. Since binary operations can require more complex logic and digital filter operations require a minimum number of samples depending on the order (moving average, Hilbert transform, low-pass filter), a producer/consumer design pattern was implemented to pack two samples at once. Every other clock cycle, two samples were pushed to a queue which could be de-queued in another timed loop that has twice the amount of time between clock cycles; the frequency of this loop is now half of the original. Instead of being limited to a 4 ns (for a 250 MHz sampling rate) propagation delay for logic circuits, 8 ns provided more freedom and less restriction on what could be computed. In order to do this, however, two samples must be taken at a time and processed each clock period to avoid overflow. For SS systems, an acquisition engine was used to ensure reference-triggered acquisition would be possible due to the operations of an SS system using a polygon mirror. A reference-triggered acquisition includes pre and post-trigger samples in situations where the trigger does not indicate the start of the acquisition but some location thereafter. The FPGA processing diagram is shown in Fig. 3.1. Raw samples are first acquired from four channels as described above and sent to the acquisition engine. The phase from the k-clock signal is then extracted using a Hilbert transform (configured with Xilinx CORE generator) with 89 coefficients followed by the arctangent of the imaginary and real components (Xilinx LogiCORE IP CORDIC). The number of coefficients for the Hilbert transform was chosen to achieve accurate phase unwrapping in the range of the k-clock fringe. The fixed-point data type word and integer length (radix point, location of decimal) were chosen to be as small as possible to use less FPGA

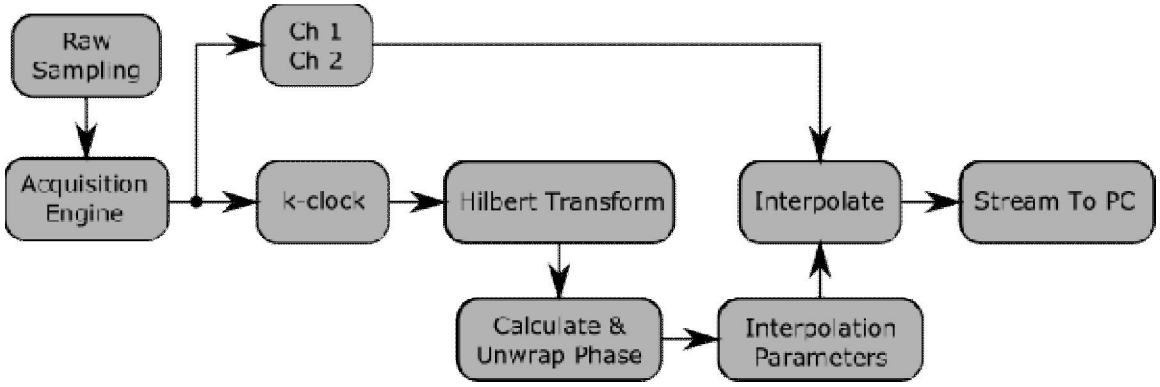

Figure 3.1 Flowchart of FGPA Implementation.

resources but large enough to not lose information that was acquired. This was done empirically by measuring the input and output of the algorithms with no operation, only conversion from 16-bit integer to 16-bit word length and 2-bit integer length which determined the location of the radix point. Lastly, the two polarization channels are interpolated with an interpolation factor to produce the desired number of points in an A-Line.

3.4 Acquisition & Real-Time Resampling

A Mach-Zehnder interferometer (MZI) is used for triggering an A-Line acquisition in the PS SS OCT system and providing a k-clock for real-time resampling. The trigger for the SS system is the power level indicator output of the MZI. Once an A-Line is triggered, the acquisition engine begins. The method used for real-time resampling is based on a k-clock from an MZI. A diagram for a basic bulk MZI is shown in Fig. 3.2. An MZI is similar to a Michelson interferometer except that instead of reflecting the two arms back to the first beamsplitter for interfering, they are instead transmitted and combined in a second beamsplitter. The glass in Fig.

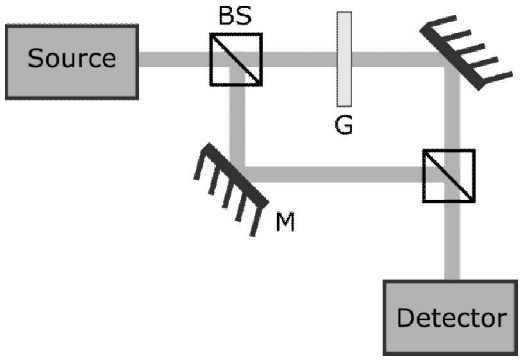

Figure 3.2. Schematic of Mach-Zehnder interferometer where BS, beamsplitter; M, mirror; G, glass for optical delay

3.2 is used to delay one path by a fixed amount. This could also be accomplished in a fiber-based MZI by having one arm have a longer fiber length. The frequency of the fringe produced on the MZI k-clock output is related to the optical path difference of the two light paths. An example of a k-clock signal with its unwrapped and interpolated phase is shown in Fig. 3.3. The information from the MZI is used for real-time sampling in the k-domain. Early works modified scanning waveform to produce linear-in-k spectrum [29] which requires calibration and daily adjustments. For SD systems, a compensation prism has been shown to be effective [30]. For SS systems, using an MZI allows for the sample clock to be an external trigger locked to the zero-crossings of the MZI. This rate was doubled by using the quadrature MZI signal from the Hilbert transform [31]. One disadvantage of this method is that the sampling rate is fixed and limited to the frequency of the MZI output and the maximum rate allowed by external triggering, which is less than the maximum sampling rate if using only internal clock sources. More recent approaches have exploited the phase information of the MZI output [32] and with the implementation of FPGAs [33] a robust, accurate and fast methods for real-time resampling is possible. I used a modified version of this method and extended it to polarization-sensitive systems sampling both

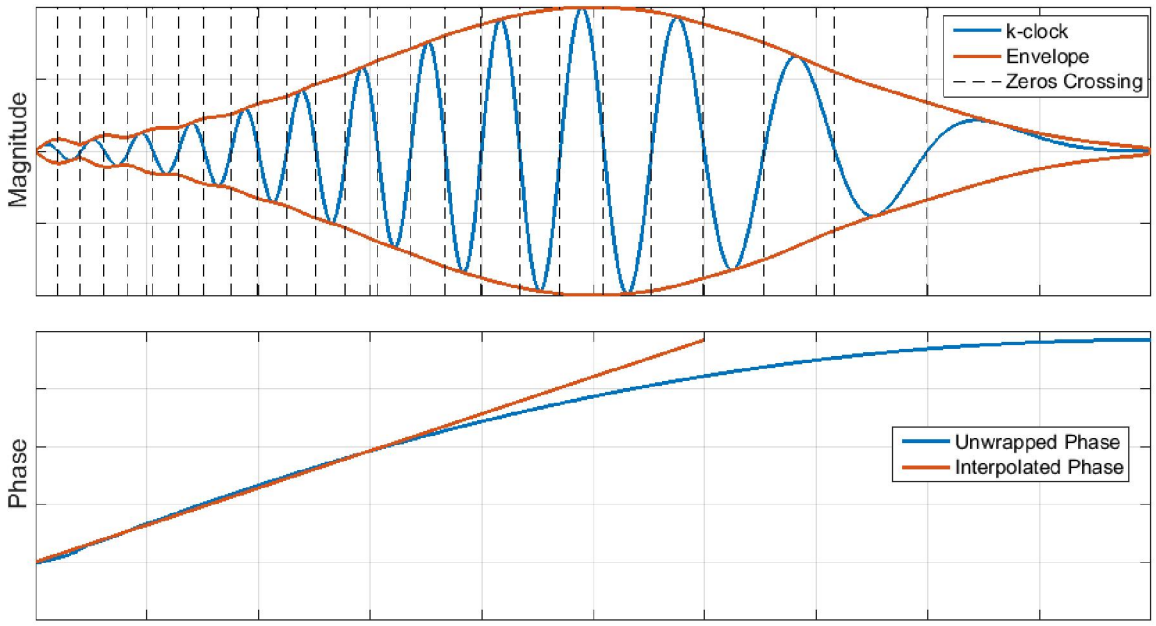

Figure 3.3. Simulated k-clock signal to demonstrate the nonlinear fringe pattern and it's unwrapped phase. The vertical dashed lines indicate zero crossings.

polarization OCT channels, the MZI output as well as the power indicator at 250 MHz with a sustained throughput of ~700 MB/s. Once the phase is unwrapped it is multiplied by a constant factor (to determine number of points in A-Line) and monitored until the difference from the current to previously used data point is one "degree" larger. The previous and current points are then used to linearly interpolate the location of one "degree". An increment of one was used to simplify the logic processing required and in some cases use existing optimized logic slice (DSP48E1). The current point is then used for comparison for the following point, and so on. This system was used at its lower rate (50 MHz) for tracking facet capsule in the spine [34]. With the current configuration, a maximum throughput of 1.1 GB/s is possible but is not sustainable for continuous recording. Computer RAM limitations on the acquisition computer as well as hard disk write speeds will limit how much data can be acquired before an overflow would occur.

Currently, only solid-state hard drives in a redundant array of independent disks (RAID) 0 (alternately writing to each disk) configuration can sustain throughputs of 700 MB/s.

3.5 Alternative Algorithms & Architectures

An alternative to resampling and then computing the FFT is to do it all in one algorithm with a non-uniform FFT (NUFFT) [33, 35, 36]. Implementations on FPGA have shown promising results but one disadvantage is not having access to raw recorded data for post processing of FFT using higher precision data types. Images meant for thorough analysis will still require the raw data recorded prior to the NUFFT operation. This could be beneficial, however, to stream NUFFT output for display while streaming the raw data to be saved. Sending data only for display will limit throughput but still have access to raw, un-interpolated data.

FGPAs have been the primary component used for real-time OCT processing until the past several years. The low-level nature of FPGAs make programming, troubleshooting and compilation rather challenging. One solution to this problem was the introduction of graphics processing units (GPU) for signal processing. The use of GPU processing for OCT has been increasing as it is powerful and simple to use [37]. Scalability has become an important factor in high-performance computing as faster computation is expensive and the reusability of hardware and software when other components are updated simplifies upgrades. Several comparisons of FPGA and GPU methods for OCT have been reported [38-40]. Generally, while GPUs have greater clock speeds and fast FFT calculations, large data chunks need to be sent to the GPU to start seeing benefits. FPGAs remain faster for interpolation and currently there is less overhead in data transfer between the FPGA and the PC. Lastly, new compression algorithms have been

introduced to gain even more speed by using less data through compressed sensitive paired with GPU processing methods [41].

3.6. High-Speed Functional Imaging

Moving into functional imaging, FPGAs are useful to maintain synchronization and pipeline processing to provide real-time feedback such as Doppler tomography [21, 42]. With higher sampling rates, tight synchronization of scanning, stimulation and recording becomes more important to reduce jitter and scrolling errors that can occur if unsynchronized clocks are off by even a part of a cycle.

3.6.1 Timing and Dual-Wavelength Systems

In some cases, OCT imaging at more than one wavelength-region is beneficial to gain extra information about a sample [43, 44] or when using optical markers such as some voltage-sensitive dyes during functional imaging. The tight synchronization required by functional imaging that was developed was extended to include a second OCT system at a different wavelength. To maintain synchronization, the two OCT systems need to have the same A-Line rate or be a multiple of each other. For SD OCT systems, the master clock was chosen to be one of the frame grabbers since it is the site of limiting frequency in the system and depending on the frame grabber used, it is the only clock that can be used for acquisition. The clock from the acquisition device, frame grabber or digitizer, determines the speed for the rest of the system and can be made available to other cards on acquisition computer. This is not necessarily true for the reverse. Using the acquisition device as the master clock, galvo/stimulation signal control and

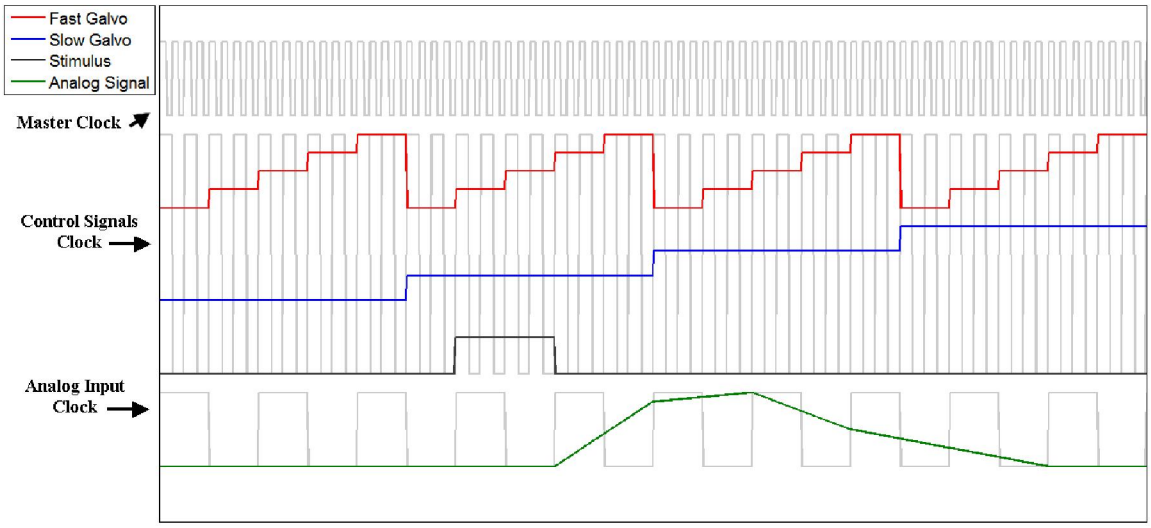

Figure 3.4. Example of a timing diagram for synchronized OCT system. The master clock is provided by the acquisition device and the control signals and analog input clock divide the master clock to obtain the desired rate.

analog acquisition were all based on divisions of this clock. A timing diagram is provided in Fig. 3.4 with the respective signals displayed for clarity. The clocks for the second OCT system are not shown since they would be similar to the existing figure, the clock would just be different by a multiplier. It is worth noting the signals for the galvo scanners are not smooth ramps to reduce possible fringe washout during acquisition of an A-Line. Therefore during acquisition of each A-Line, the galvos are not moving. However, at faster scanning speeds the galvo position will most likely trace a saw-tooth waveform.

Lastly, an area camera was used as a line scan camera for OCT imaging. The advantages of using an area camera are simplifying alignment and collecting more light by using vertical binning. As will be shown in Chapter 4, choosing detection arm optics for SD systems to focus the spectra on more than one pixel height will result in significant gains in the SNR at a small cost to the max

acquisition rate. The area camera-based system was demonstrated for measuring Faraday rotation at multiple depths using phase information of SD OCT complex depth profiles [45].

3.6.2 Directed Scanning & Features

In addition to the high-speed real-time OCT setup for SS and SD systems, once these systems are configured, they are flexible to change scanning behavior, timing and real-time sample exploration using a directed scanner. An example of the front panel display for customization is in Fig. 3.5. The intervals in-between A-Lines and in-between B-Lines can be modified to reducing scanning artifacts and in the case of fast cross-sectional scanning for function, a triangle wave can be used to eliminate the need to quickly return the scanner to the starting position, which would be the case if a ramp control signal was used. To further stabilize scanning, a sigmoidal decay can be included if there is an interval allowed between cross sectional scans that remove discontinuous jumps from a saw-tooth waveform at high scanning speeds. The timing resolution of the master clock can be modified to save computer RAM with maximum rate 2 MHz. This means the multiple for all control/recording channels is limited to 500 ns to maintain synchronization.

The organization of the acquisition program is optimized to stream cross-sections for processing and storage. When the cross sections are small, such is the case in 3D functional imaging, the architecture of the program can change on-the-fly to accommodate switching between cross-sectional imaging and 3D functional imaging. When choosing imaging locations for functional imaging, a stable depth profile with a high SNR is most desirable. In order to investigate potential locations in real time without moving the sample, thereby maintaining the ability to track all

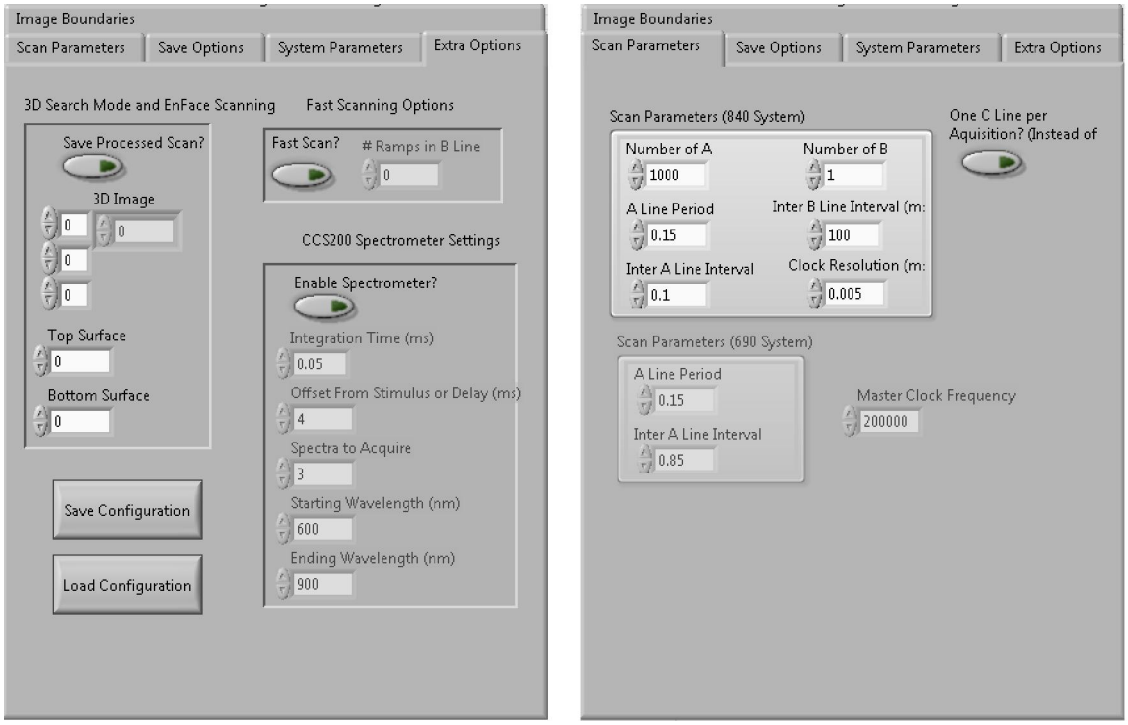

Figure 3.5. The front panel of the acquisition program demonstrating some of the options and parameters that can be used to customize acquisition.

locations in relation to the sample throughout an experiment, a real-time directed scanner was implemented. An example of the scanner display in the acquisition program is shown in Fig. 3.6. Prior to directed scanning, the imaging boundaries need to be determined and an entire 3D volume is acquired. The volume is then integrated in depth to produce an *en face* image providing a top-down view to aid in locating potential recording sites. If only a specific depth is desired for *en face* images, it can be set in the front panel of the program shown in Fig. 3.5. During acquisition, the galvo position can now be changed in both x and y directions and an updated cross-section, modulated spectra and depth profile are displayed.

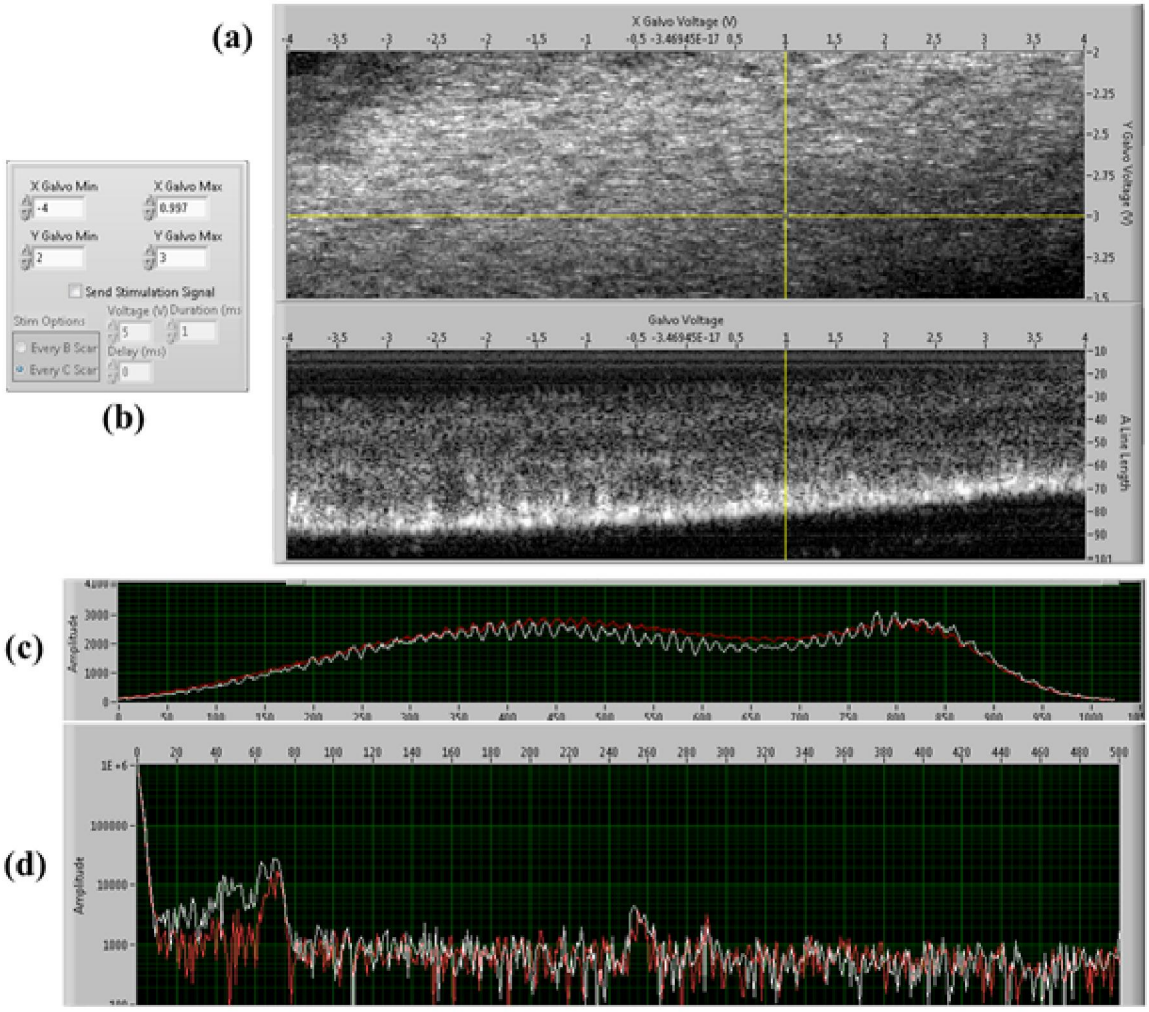

Figure 3.6: Display windows using a salamander retina as a sample. (a) en face (top) image of photoreceptor layer and cross section (bottom) image of the retina. The yellow are the current scanner location which is controlled with voltages ranges in the control signal panel (b). (c) The spectra and (d) calculated depth profile for a PS system for selected A-Line.

Chapter 4

Balanced Detection for SD OCT[1]

4.1 Overview

Increasing sample rates can result in reductions in SNR and with common noise sources from the light source, auto-interference and DC, the image can be degraded further. We present a new design for SD OCT that allows balanced detection using a single camera. The design uses polarization optics to encode the light in reference and sample arms. Two parallel and highly aligned spectra, which carry out-of-phase interference signal, in-phase common noise and auto-interference terms, are focused on the camera that performs the digital balanced detection for each wavelength. Since the camera used for this system is an area camera, the spectra can be focused onto more than one row of pixels. This makes vertical binning possible which can significantly increase the SNR of the system dependent on the number of vertical lines used for binning. The optical system is characterized and tested for tissue imaging. Results demonstrate consistent signal gains in depth and suppression of DC and sample auto-interference. The design could be amended further for polarization-sensitive imaging, and might provide a basis and

[1] The contents for this chapter are based on a previous publication, "Polarization-based balanced detection for spectral-domain optical coherence tomography"

demonstrate a market for manufacturing dual-line cameras with analog balanced detection capability.

4.2 Introduction

High-speed OCT has benefits in reducing signal degradation from fringe washout (noise and motion artifacts) which helps in all spatial dimensions of an OCT image. One dimensional (M-Mode, no galvo scanning) scans in time can be subject to fringe washout as well as cross sections and 3D volumes. In 2D and 3D images, if there is too much time in between scans, inaccuracies can arise in the morphology of the image from motion artifacts, impacting the representation of the sample even further. The advantages of high-speed imaging extend to functional imaging as well. Capturing fast biological signals require greater sampling rates, on the order of a millisecond, to record from a single location, cross section or volume. When imaging deeper structures in an OCT image, an increase in SNR will make deeper structures more visible. In this chapter, increasing SNR by using a balanced detection scheme, the signal can be doubled while common noise sources are suppressed and A-Lines are acquired at high-speed.

Relative intensity noise (RIN) is one of the most significant factors limiting the sensitivity of an OCT system [46]. RIN suppression from balanced detection has been shown to improve SNR in TD OCT [47] and it is required to maintain a shot-noise limited system in SS configurations. SD OCT imaging rates have reached over 300,000 axial scans-per-second and continue to increase [26, 27], making RIN a significant factor meaning system performance would benefit from balanced detection [48]. Balanced detection also has the additional benefits of removing DC components (signal at zero depth) from OCT images and reducing auto-interference (sample

interfering with itself) terms. This allows for imaging in shallower areas that might be otherwise masked by large DC or auto-interference signals. It is possible to image in deeper regions but it is known that the SNR for SD OCT decays with depth making this option undesirable. Without balanced detection, DC and auto-interference reduction has been accomplished by phase-shifting the spectra using a scanning delay line, piezo translator or phase modulators that require at least two axial scans [49-51]. Requiring several scans for one A-line is not very desirable for functional imaging where time between scans is important and may require more optical power from the light source since exposure times may have to be cut in half. However, an advantage of those methods is in realizing full range OCT which doubles the available imaging depth.

Since TD and SS systems are photodetector-based, differential measurements required for balanced detection can be easily implemented [47, 52]. SD systems, on the other hand, rely on a spectrometer for detection, making a true analog balanced detection nearly impossible with conventional designs since they typically use a CMOS or CCD camera. Balanced detection systems for SD OCT support real-time imaging of a sample and reduce fixed-pattern lines, sample auto-interference and DC component. Balanced detection has demonstrated significant signal improvements over standard single camera methods [53, 54] but require a second set of detection optics which contributes to a source of error when comparing spectra from each camera and is costly to implement. Investigation into the benefits and disadvantages of BD SD OCT and its effects on noise levels has also been examined. Despite the two carefully calibrated spectrometers, ~40% residual excess photon noise was not canceled [54]. The authors also pointed out large degradation of SNR improvement along the imaging depth, since it is hard to achieve 180º phase difference between two individual spectrometers for interferograms with high

modulation frequencies. Area camera configurations have been used to remove auto-interference [55] as well as for balanced detection [56] but the returning light does not have an identical path through the detection optics and acquisition rates are on the order of a millisecond.

In this paper, we report a novel BD SD OCT system that encodes the light in reference and sample arms with polarization states. The BD OCT couples the light returning from the sample and reference arms into separate channels of a single polarization-maintaining (PM) fiber that delivers light to the detection unit without mixing. The BD SD OCT system was designed, constructed and characterized for two different configurations for the detection optics that performs the mixing for balanced detection; one using a Wollaston prism and the other a calcite block. Description, characterization and imaging performance of both designs are given in the following sections.

4.3 Materials and Methods

4.3.1 System Description

The BD SDOCT system is depicted in Fig. 4.1. A superluminescent diode (SLD, Broadlighter S840, Superlum, Ireland) emits low-coherent light at a center wavelength of 840 nm with a full-width-half-maxima (FWHM) bandwidth of 50 nm resulting in an axial resolution of ~5.5 μm in tissue (using 1.4 as the refractive index of tissue). Light is collimated and polarized linearly before splitting into the interferometer arms. Instead of a conventional 2x2 beamsplitter, the

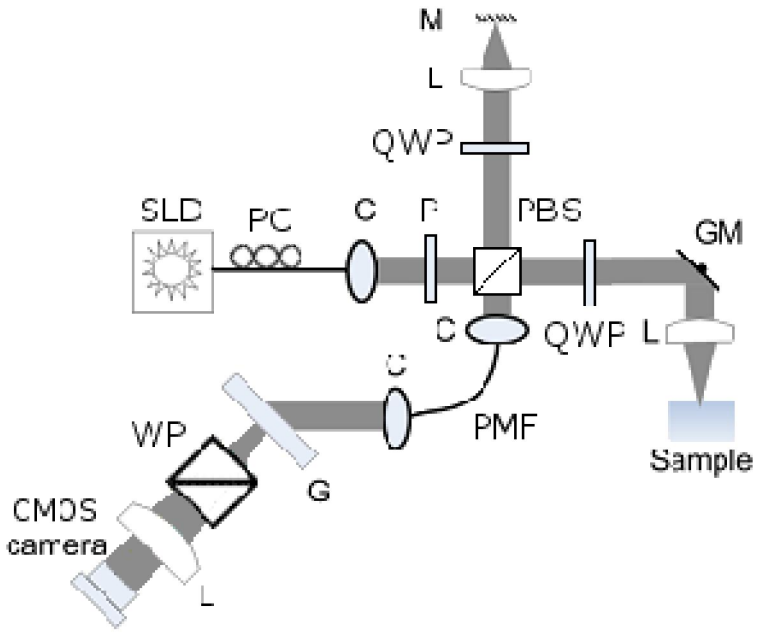

Figure 4.1. Illustration of the BD SD OCT system. SLD: superluminescent diode; PC: polarization controller; C: collimator; P: polarizer; PBS: polarization beamsplitter; QWP: quarter-wave plate; L: lens; M: mirror; GM: galvo mirror; PMF: polarization-maintaining fiber; G: grating; WP: Wollaston prism.

design utilizes a polarization beam-splitting (PBS) cube, which directs linearly polarized orthogonal states to the reference and sample arms. The splitting ratio of sample to reference powers was set to 99:1 by adjusting the axis of the input polarizer resulting in 15 mW in the sample arm and 0.14 mW in the reference arm. It is worth noting that changing this ratio to 90:10 or 50:50 is quite easy and we have not observed a significant effect of the splitting ratio on the system performance (SNR, auto-interference or DC reduction, etc.) for the studies reported here.

The reference arm consists of a quarter-wave plate (QWP), an achromatic lens and a back-reflector, which is the front surface of a 10° wedge prism. Because the axis of QWP is oriented at 45° to the incoming polarization state, light double-passing through the QWP returns to the PBS cube with its linear polarization rotated by 90°. This operation can be written by using the Jones

calculus as $J_{QWP}^{T} * J_{QWP} * E$, where E is the electric field vector $[0\ 1]^{T}$ representing the vertically polarized light entering the QWP, J_{QWP} is the Jones matrix of the QWP with axis oriented at 45° which is $(1/\sqrt{2})[i\ \ 1;\ 1\ \ i]$ and ^{T} is the transpose operator. As a result, the reference light after its second pass through the QWP becomes horizontally polarized, $[1\ 0]^{T}$ and transmits through the PBS toward the polarization-maintaining-fiber (PMF).

The sample arm includes a QWP, a galvanometer-based scanner and a scan lens that focuses light on a target. Horizontally polarized light from the PBS enters the QWP. The axis of the QWP is set to 45°, which creates circularly-polarized light propagating toward the sample. In this study we assume isotropic or low-birefringent tissues to demonstrate the BD approach in SD OCT, but the approach can be extended to polarization-sensitive imaging as launching circularly-polarized light on birefringent samples is common practice in polarization-sensitive OCT [57]. To extend the system for polarization-sensitive imaging, the polarization component directed to the source arm would also need to be mixed with reference light. This could be accomplished by using a circulator prior to the PBS and orienting the reference arm quarter-wave plate to 22.5° to provide the components for interference in a second balanced detection path. The scan lens (LSM03-BB, Thorlabs, Newton, New Jersey) with 36 mm effective focal length produces a lateral resolution of ~15 μm. Light back-scattered/reflected from the sample completes another pass through scan lens and the QWP. Then, the PBS cube reflects the returning vertical state toward the PMF.

The returning light from each arm is spatially combined at the PBS, but interference does not occur as the electric fields of the reference and sample light oscillate in orthogonal directions. The PMF, a 10 m segment with FC-APC connectors on both ends, is aligned to ensure that the reference light couples to one of its polarization channels (i.e. slow) and the sample light couples

to the other channel (i.e. fast). To aid in optimum alignment, a half-wave plate rotating the polarization states can be placed before the PMF. As such, the only role of PMF is to transmit light to the detection unit and maintain the linear polarization states propagating through its core.

4.3.2 Spectrometer Design

In the detection arm, light emerging from the PM fiber is collimated by a 50 mm achromatic lens and launched at a transmission grating (1200 lines/mm Wasatch Photonics, Logan, Utah). The FC-APC connector of the PM fiber is rotated with a rotational stage so that the emerging polarization states are at ±45° to the vertical grating lines. This reduces any polarization effects of the grating. To get interference to occur, one would extract and combine the projections of the orthogonal states, for instance by using a polarizer transmitting one projection and eliminating the other. In our design this task is performed either by a Wollaston prism or by a tilted calcite block to utilize both projections for balanced detection. Fig. 4.1 shows the Wollaston prism angularly splitting (0.5°; Karl Lambrecht Corp., Illinois) these projections. Consequently, interference-related oscillations can be observed on two spectra. A 200 mm achromatic lens is used for focusing two highly aligned and parallel spectra on a camera sensor. Instead of a dual line scan camera, we used an area camera (2048x1088 pixels, acA2000-340kmNIR, Basler, Ahrensburg, Germany) that allows selection of two lines. Using the area camera ensures synchronization of the spectra, simplifies alignment and configuration of the detection arm (only requiring one set of detection optics) and allows for variable vertical binning to acquire the full spectra even when the camera is slightly tilted with respect to the spectral lines. Spectra were acquired with an exposure time of 25 µs and a window of 4x2048 pixels for each spectra. The maximum line rate for the camera with the given window is 5.6 kHz and up to 10 kHz with 1x2048 pixels per spectra. The

pixel size of the camera is 5 μm x 5 μm and the theoretical (Nyquist) maximum depth, z_{max}, is calculated to be 4.5 mm in air. Data were acquired with a camera link image acquisition card (PCIe-1429, National Instruments, Austin, Texas) and custom LabVIEW software.

The detection unit was also designed with the use of a 5 mm thick calcite block instead of the Wollaston prism. The calcite block was placed between the focusing lens and the camera with its birefringent axis aligned at ±45° to the linear polarization states. Approximately 4° tilt about the horizontal axis (normal to the incident beam) was introduced to separate the spectra. According to the Snell's law, the tilt provides different paths in the birefringent media for the projections of the polarization states leading to interference and a slight separation (~20 μm) between the spectral lines. The small difference in optical paths might focus the spectra unequally, which could be avoided by tilting the camera. Nevertheless, the slight separation of the spectra supports nearly identical wavelength to pixel mapping on the camera for balanced detection, which is important for imaging at deeper depths, removing common noise and maintaining the spectra phase alignment to be 180° out-of-phase.

To achieve out-of-phase alignment of the spectra, the Wollaston prism or the tilted calcite block was fixed on a micrometer-controlled goniometer. Then, a coverslip sample was imaged in real time. The goniometer was rotated until the auto-interference peak (interference of front and back surface of the coverslip) was minimized. The axis of rotation of either element was the direction of the incident light.

4.3.3 Image Formation

In SD OCT systems, sample and reference arms interfere and their optical path difference encodes the depth information into modulations on the source spectrum [18]. To recover the depth profile, the spectrum is first interpolated from its original wavelength mapping to k-space. Then taking the inverse Fourier transform of the interpolated spectrum produces the complex depth profile $A(z)exp(i(\phi(z)))$ where A is the amplitude at depth z and ϕ is the phase of the modulation. The reflectivity of a sample at a particular depth is proportional to the magnitude of the complex depth profile squared, $R(z) \propto A^2(z)$. Reflectivity is the conventional OCT contrast. It is usually plotted in logarithmic scale with consecutive A-lines acquired during a scan to produce a tomographic image.

In BD OCT, there are two spectra each of which contains light from the reference and sample arms. The interference related oscillations on these two spectra have a phase offset of 180°. In other words, a constructive interference at a particular wavelength/pixel of one spectrum corresponds to a destructive interference of the same wavelength on the other spectrum. On the other hand, auto-interference of the sample light, common noise and DC terms from the source are simply present on both spectra without any phase difference. Therefore, subtraction of two spectra will cancel the undesired components while doubling the OCT signal.

4.4 Results

4.4.1 Proof of Principle

Demonstration that the interference related oscillations on acquired spectra are out of phase and the balanced detection by spectral subtraction doubles the signal is shown in Fig. 4.2. The interference pattern is for a single reflector, as the front surface of a wedge prism was utilized as the sample. The interference pattern on the area camera is shown with the calcite block (Fig. 4.2(a)) and the Wollaston prism (Fig. 4.2(b)) configurations. The latter shows the modulation for a lower frequency which corresponds to a shallower depth. The spectral lines with the Wollaston prism configuration are plotted in Fig. 4.2(c). Each trace is with a vertical binning of 4 pixels. The spectral modulations in Fig. 4.2(a)-(c) are observed to be 180° out-of-phase. It is worth noting that the shapes of the spectra are not exactly the same; the blue signal in Fig. 4.2(c) is slightly larger than the green signal. This has the largest effect on DC reduction after the BD calculation. Possible sources of the amplitude mismatch could be due small misalignments of optics and imperfect optical elements including their wavelength dependencies. There are several compensation methods used in literature to correct this difference which have been shown to significantly reduce the DC component [53]. The subtraction of both spectra, producing the BD signal, is presented in Fig. 4.2(d) without applying any correction method.

The vertical spacing of the spectra on the area camera was adjusted by changing the tilt of the calcite block before the camera. The rotation of the calcite block was optimized such that the spectra recorded were completely out-of-phase as described in the previous section. For the Wollaston prism configuration, accurate rotation of the prism was also done to ensure out-of-

phase spectra. The spacing between the spectra for the Wollaston prism case was 825 μm while the calcite configuration places the spectra much closer (~20 μm) as seen in Fig. 4.2(a),(b). Since the performance of both the Wollaston prism and calcite-block configurations were similar, the results in the next section are derived from the Wollaston prism configuration.

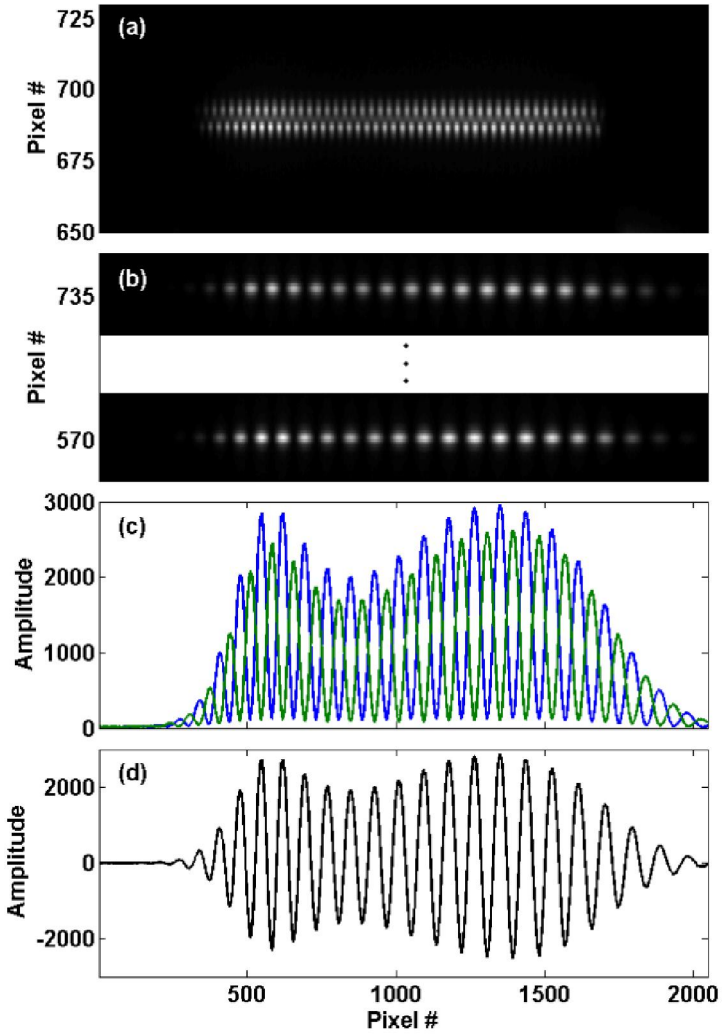

Figure 4.2. Spectral lines and modulations on the camera for a single reflector. (a) A section on the area camera shows two spectral lines selected for balanced detection for the calcite block configuration. (b) Area camera regions covering the two spectra from the Wollaston prism configuration. (c) The modulations are completely out-of-phase. (d) Subtraction of the two spectra yields the balanced detection signal.

4.4.2 Performance

Sensitivity of the BD system was measured to be 106 dB by adding the SNR of 68 dB and attenuation of 38 dB. The observed sensitivity includes the 3 dB contribution from balanced detection (two channels) and about 4.7 dB measured contribution from vertical binning of 4 pixels in software. The detection optics are typically configured to focus the spectra on the pixels of a line scan camera. Using an area scan camera, the spectra can be focused on several rows of pixels. This enables recording greater signal levels, increasing SNR. The SNR gains would have to be balanced to the extra cost of imaging speed. The maximum gain expected from a binning of 4 pixels would be 6 dB. The SNR for the OCT system was calculated by the ratio of the peak from a wedge prism at 330 μm and the average noise level between 400 μm and 3 mm. Attenuation was calculated by measuring the power at the fiber tip of the detection arm with a mirror as the sample with and without a neutral density filter to prevent camera saturation. The ratio of the unattenuated and attenuated cases results in power values of 9 mW and 1.5 μW, respectively.

Fig. 4.3 shows the single channels and BD signal from a wedge reflector at several depths. The traces are normalized to the BD peak at 110 μm. The single channel magnitudes differ slightly in depth due to a mismatch between the spectral magnitudes mentioned above. Also, depth-dependent decay for Channel-2 (green triangle marker) is slightly less when compared to Channel-1 (blue square marker). However, gains in the BD signal (red circle marker) are consistent in the depth range measured. Overall, the signal improvements over Channel-1 and Channel-2 were respectively 5.1 ± 0.3 dB and 6.8 ± 0.1 dB for the mean and standard deviation. The signal improvement compared to the averaged depth profiles results in 5.88 dB, which is

close to the theoretical value of 6 dB. The improvement for the last depth location in Fig. 4.3 (5.7 dB at 1630 μm) was only 0.3 dB smaller than the one for the first depth location (6 dB at 110 μm). The farthest location recorded was 2.64 mm (not shown) that resulted in an SNR of

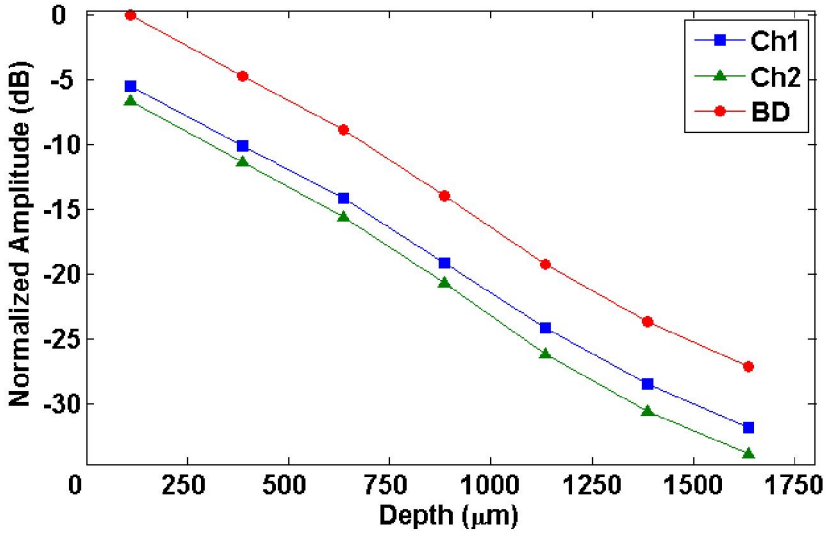

Figure 4.3. Improvement of the BD operation over the single channels (Ch1 and Ch2) is maintained within the imaging depth. SD-OCT is subject to a depth-dependent decay as expected.

32 dB including the BD gain of 5.7 dB. Therefore, the signal improvement of balanced detection by this design does not degrade significantly with depth.

To demonstrate system performance regarding DC and auto-interference reduction, a glass coverslip was imaged. Fig. 4.4 shows the front and back surfaces of the coverslip at 150 μm and 400 μm, respectively and the auto-interference peak of these surfaces is at 250 μm. Comparison of the single channel and balanced detection signals at these locations shows that the balance detection enhances the peaks for the front and back surfaces by about 6 dB and suppresses the auto-interference peak by about 17 dB. A double-reflection peak at 500 μm is also suppressed to

the noise level. Fig. 4.4 also shows an increase of the noise level for the BD trace. There is an expected increase in noise level in the BD signal compared to single detection but the increase is

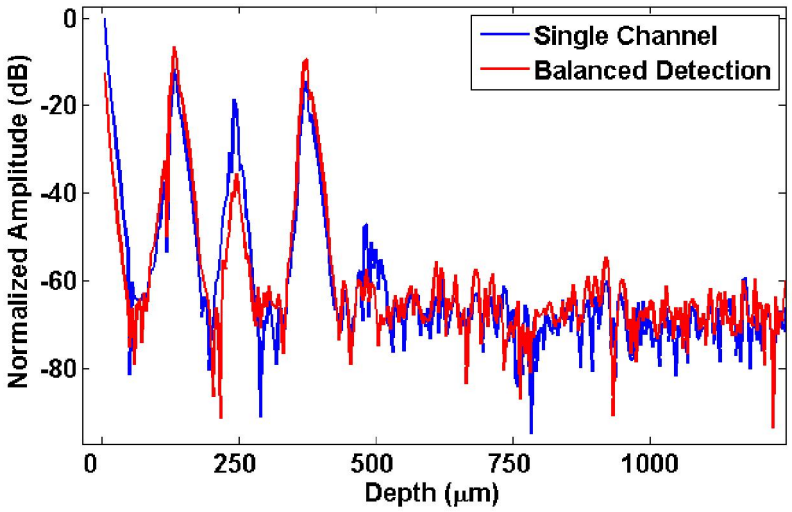

Figure 4.4. Logarithmic depth profiles of a coverslip sample. Signal gains by balanced detection for the front and back surfaces are represented by peaks at 150 μm and 400 μm, respectively. Auto-interference (250 μm) of these surfaces and DC terms are suppressed. The peak at 500 μm is due to multiple reflections within the coverslip and only visible on the single channel. Single channels were similar so only Ch1 is displayed.

shot-noise limited, possibly due to using only one camera for detection circumventing the complications of two camera configurations since only one sensor is the source of noise. Assuming a shot-noise limited system, the increase in the noise was $\sim\sqrt{2}$, as expected. The 3 dB increase in noise and 6 dB increase in signal results in a net gain of 3 dB for the SNR of the reflectivity signal. For Fig. 4.4, it is important to note that the coverslip was positioned to maximize the auto-interference term to demonstrate the full effect of balanced detection for reducing auto-interference. The reduction of the auto- interference signal ranged from 12-18 dB.

The DC artifact at zero was reduced by 15 dB. These numbers are obtained without employing any software correction method to indicate the performance of the hardware design.

4.4.3 Biological Tissue Imaging

The performance of the BD system on biological samples was accomplished by imaging a rat eye *ex-vivo*. Cross-sectional images of a rat eye were acquired with 500 A-lines. Fig. 4.5 demonstrates the image reconstructions from a single channel, spectral addition and spectral subtraction (balanced detection) for Wollaston prism and calcite block configurations. The same color index values are used on all images for comparison. The dynamic range for the reflectivity images is 40 dB.

The cornea, iris and a portion of the lens are apparent in Fig. 4.5. The images also contain DC, horizontal lines and auto-interference (AI) as labeled in one of the single channel images (Fig. 4.5(d)). Addition of the spectra should remove the signal and double the common terms. However, the images of the eye in Fig. 4.5(b),e are not completely removed because of the small imbalance between the spectral magnitudes. The common terms (DC and auto-interference) in the image are more prominent, as expected. The structures in the BD images (Fig. 4.5(c),(f)) are brighter than the single channel images (Fig. 4.5(a),(d)), because the BD operation doubles the signal. The background noise, on the other hand, is also increased relatively less as previously described. Moreover, the DC artifact and the auto-interference terms from the cornea and iris are virtually eliminated in the BD images. Therefore, the BD system allows the use of shallow regions for SD OCT imaging. Most of the horizontal lines are eliminated by the BD operation. The line at the bottom of the image, on the other hand, persists in the BD images. This might

suggest a cross coupling between the orthogonal channels due to imperfect optics and/or alignment and a delay corresponding to the location of the line. The length of the PM fiber and its

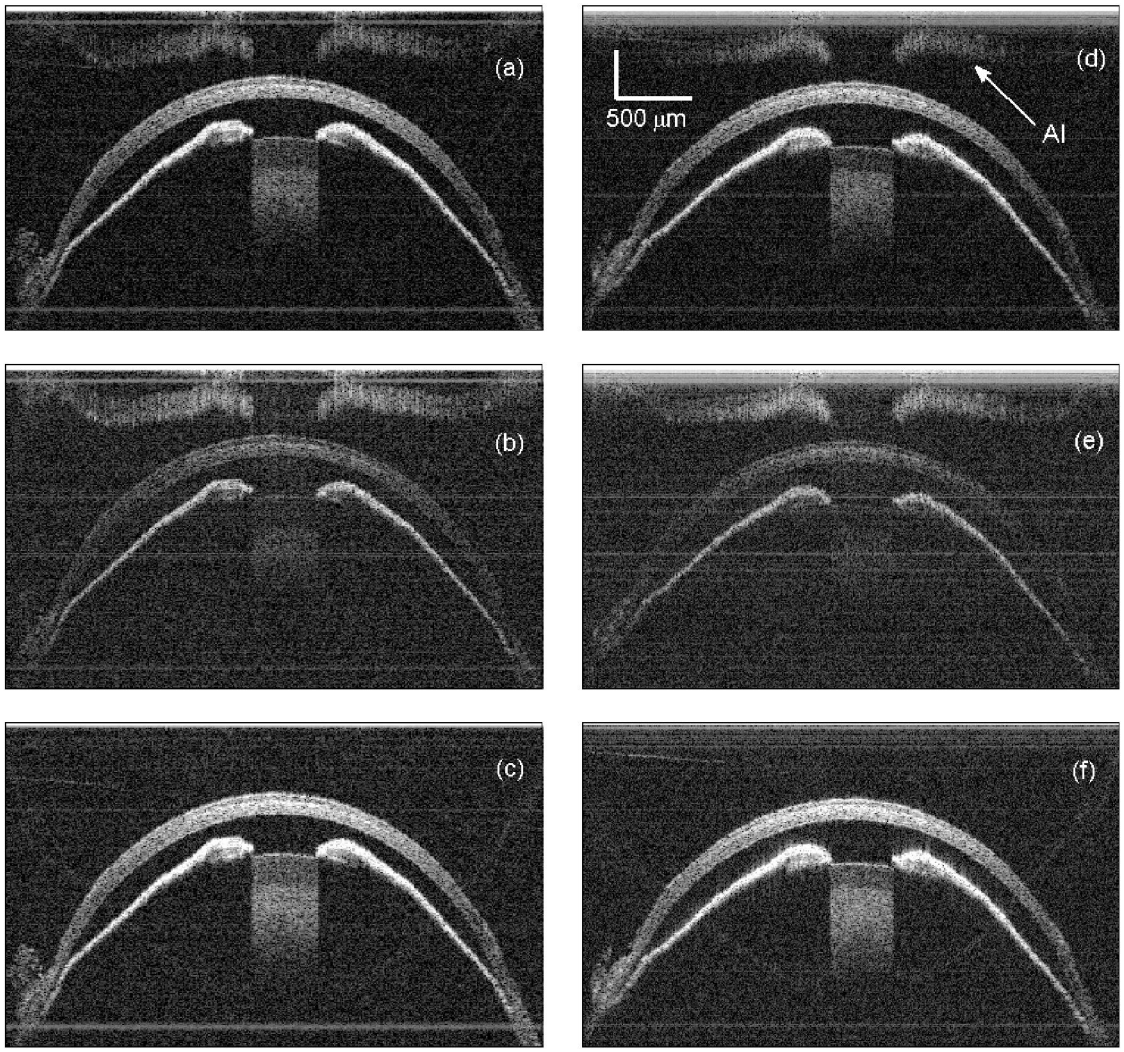

Figure 4.5. Rat eye images with the Wollaston prism (a,b,c) and calcite block (d,e,f) configurations. (a,d) non-balanced detection (single channel) images, one of which (d) contains label for auto-interference (AI). (b,e) addition of spectra shows imbalance in signal and highlights the common terms. (c,f) Common terms and fixed-pattern lines are removed and the signal is doubled with balanced detection.

birefringence can affect or decide the location of such a line, which can also be removed by background subtraction.

4.5 Discussion

The advantages of our BD SD OCT system lie in the polarization-based design. Light that forms two parallel and highly aligned spectra propagates through the same optical elements in the detection arm. This contributes to the stability and provides consistent signal gain over the imaging depth. The spectrometer has a single fiber input and only one camera, which eliminates synchronization issues for digital BD operation that might occur between line acquisitions if a two camera setup is employed. Moreover, the analog circuitry of the camera sensor could be manufactured to provide a differential signal using CMOS technology. This would provide SD OCT with balanced detection in analog domain that would increase SNR and dynamic range compared to the existing setups.

Programming and computational costs involved with a two camera setup are avoided with our setup. Due to the hardware configuration, the acquisition speed of a two camera (line scan) setup is greater than the speed provided by the area camera that outputs two lines. However, the area camera used in this system can provide exposure times as low as 24 μs, which reduces fringe washout and suggests the use of dual-line scan cameras preferably with BD capability. Another advantage of implementing a BD system is to reduce source noise to improve image quality. The source used in this study was quite stable, however, OCT systems using noisier sources, such as a Ti:Sapphire laser, would benefit more from a BD configuration.

The design presented here allows for balanced detection in SD OCT, but can also be extended to its Doppler and polarization-sensitive variants. For birefringent samples, reflectivity measurements can be made accurate if the OCT system detects two orthogonal polarization channels. This is achieved by PS OCT systems, which also provides additional contrasts for imaging tissue anisotropy. The BD system described here launches circularly polarized light on the sample as in many PS OCT implementations; however, a second detection path is needed to capture the cross-polarization information. This can be implemented using another BD spectrometer, which would receive reference light and sample light circulated from the source arm. Fiber-based implementations have some advantages over the bulk systems. Replacing the PBS cube with a PMF-based polarization splitter/combiner would allow more flexibility and freedom for configuring a BD system. However, using such a fiber splitter/combiner could induce ghost lines due to polarization leakage in the component and approaches to remove the ghost lines would be needed. This could include displacing the ghost lines out of the imaging range by using longer PMF segments [58].

Our BD SDOCT system demonstrates the expected increase in signal while reducing DC and sample auto-interference terms. Signal gains are maintained in depth. The simple design and single set of detection optics makes it an attractive improvement to SD OCT imaging with further advancement possible such as PS systems and support for a dual-line camera for analog BD detection. This will help to meet the challenges of an increased acquisition speeds for SD OCT systems. The improvements would also aid in highly demanding functional imaging studies.

Chapter 5

Border Zone Imaging of Cardiac Tissue Using SS PS OCT[2]

5.1 Overview

In this chapter, we shift our focus to look at applications of polarization-based OCT imaging. A PS SS OCT system was applied to imaging biological tissue--isolated rabbits hearts with a clearing agent applied. The benefit of using OCT for this situation is observing the cleared tissue in depth. Being depth-resolved, we are able to image several millimeters into the tissue and delineate the border between perfused and nonperfused tissue. By clearing a portion of the heart that is perfused by a coronary artery, the perfused portion of the heart becomes cleared. This simulates the conditions of an infarct. Myocardial infarction, caused by a major blockage of a coronary artery, creates a border zone (BZ) between perfused and nonperfused tissue, which is believed to be the origin of fatal cardiac arrhythmias. We used a combination of optical clearing and polarization-sensitive optical coherence tomography to visualize a three-dimensional organization of the BZ in isolated rabbit hearts (n = 5) at the microscopic level with a high spatial resolution. We found that the BZ has a complex three-dimensional structure with nonperfused

---

[2] The contents for this chapter are based on a previous publication , "Visualizing the complex 3D geometry of the perfusion border zone in isolated heart"

areas penetrating into perfused tissue with finger-like projections. These “fingers” may play an important role in the initiation and maintenance of ventricular arrhythmias.

5.2 Introduction

With many biological samples, absorption and scattering can reduce the measured signal resulting in a penetration depth ranging from only a few hundred microns to a millimeter. To fully exploit the depth-resolved nature of OCT, optical clearing has been used to allow farther imaging depths, revealing deeper structures and increasing contrast. The agents first used to demonstrate this effect were glycerol and propylene glycol, applied to skin and blood [59, 60]. Clearing tissue typically involves a dehydration of the tissue in stages of increasing concentrations to prevent any torsion or structural transformations due to rapid dehydration. Replacing water with a substance of higher refractive index renders the sample more transparent, increasing the depth that will return a measurable signal. In this chapter, isolated rabbit hearts were cleared from the left circumflex (LCX) artery and the perfusion boundary was imaged in 3D using SS PS OCT. Clearing a portion of the heart through the LCX was done to clear the tissue that would be affected during an ischemic event. Myocardial ischemia is a medical condition in which the blood flow to the heart is partially or fully obstructed in one of the major coronary arteries. If the blockage is severe, the region of tissue downstream of the obstruction site will not receive blood from this artery and its capillaries, creating a region of nonperfused tissue, known as myocardial infarction (MI). In these hearts, a border zone (BZ) between the perfused and nonperfused regions is created due to differences in the perfusion levels. The BZ has demonstrated both electrophysiological and mechanical changes post-infarct in the transmural direction [61, 62]. The

existence of a lateral BZ was initially met by controversy [63, 64] and could not be easily determined with biopsy, electrograms or blood flow markers [65]. Only with the aid of magnetic resonance imaging (MRI) [66, 67] and electron microscopy [68] was it possible to observe changes in the tissue consistent with ischemic injury and a BZ. Electrophysiological changes that develop at the MI BZ are known to be a cause for serious or fatal arrhythmias [69, 70]. Although it has been demonstrated that the BZ itself plays an important role in the initiation of these arrhythmias [71], very little is known about its three-dimensional (3D) geometry and how the geometry impact arrhythmogenesis.

Imaging the 3D geometry of the BZ is possible with conventional imaging modalities such as ultrasound, MRI and histology [72]. However, the main drawback of using MRI is the limited spatial resolution (~1 mm), which prevents resolving the BZ in fine detail. The third conventional imaging technique is histology, which uses staining to reveal viable tissue. Although histology provides a very high spatial resolution (less than 10 μm), its destructive nature does not provide for the most accurate 3D reconstructions of the MI BZ. All three techniques have been used to determine the 3D structure of the MI BZ and the results revealed that the BZ changes not only on the epicardial surface but through the depth of the myocardium. The precise 3D geometry of the MI BZ in an intact heart is still unknown due to the limitations of these imaging modalities. Therefore, there is a need for an imaging technique that overcomes the spatial limitation of echocardiography and MRI while avoiding the destructive nature of conventional histology to resolve the 3D BZ geometry.

A previously developed optical clearing technique [73] was used and it has been demonstrated that up to 4 mm of transparent cardiac tissue can be imaged instead of less than 100 μm in

nontransparent tissue [74]. This optical clearing technique was then paired with OCT to nondestructively determine the complex 3D geometry of the BZ at a very fine spatial resolution (~15 μm and ~28 μm in the axial and lateral directions, respectively). A BZ was created in the isolated rabbit heart by individually perfusing the left circumflex artery (LCX) with the clearing solution, thereby creating a border between the LCX (perfused region) and the rest of the heart (nonperfused region). By using a polarization-sensitive OCT system, we found that nonperfused tissue protruded into the perfused region in a finger-like fashion; the specific geometry of these "fingers" may provide the anatomical substrate to facilitate ventricular arrhythmias in MI hearts.

5.3 Materials and Methods

The clearing procedure in described in detail in [75], the reference for which this chapter is based. Briefly, the LCX was selectively perfused with a graded ethanol series followed by a 1:2 benzyl alcohol:benzyl benzoate (BABB) solution. The rest of the heart, that is, the tissue supplied by the right coronary and left anterior descending arteries, was not cleared and thus remained in a healthy physiological condition. As a consequence, a BZ developed between the region perfused by the LCX and the nonperfused regions of the left anterior descending and the right coronary arteries. The entire procedure lasted approximately 45 min. An image of the rabbit heart prior to and after clearing is shown in Fig. 5.1. The BZ is highlighted by the white dashed line and the inset shows and enlarged view to demonstrate the detail and complexity of the BZ geometry. There is a visible distinction of perfused and nonperfused regions. The perfused region has a darker appearance as scattering is significantly decreased since the LCX perfuses tissue in the

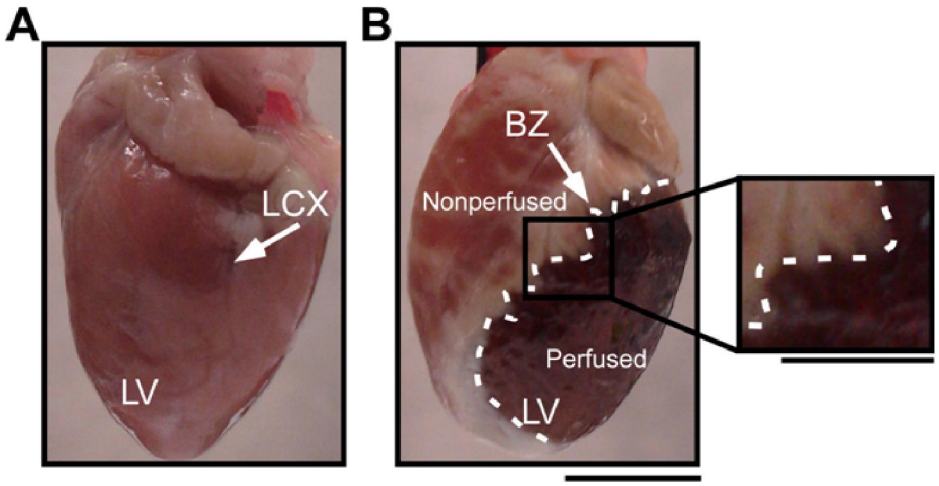

Figure 5.1. Image of the rabbit hearts before (A) and after (B) optical clearing to show the BZ. (A) Rabbit heart in the air before dehydration and clearing. (B) the same heart rotated clockwise to show the BZ after dehydration and clearing. LV, left ventricle. Scale bar = 0.5 cm.

transmural direction as well as the plane of the epicardial surface. OCT imaging of the BZ was performed three times: before the LCX was perfused with ethanol, after the LCX was perfused with ethanol and after the clearing procedure.

Imaging of the BZ under all three conditions was performed using a previously described PMF-based SS PS OCT system [76]. The system, operating at the 1300 nm region, provided axial and lateral resolutions of approximately 15 μm and 28 μm, respectively with a sensitivity of 106 dB. A two-dimensional (2D) cross-sectional image containing 1000 A-lines (depth profiles) was acquired as the beam was laterally scanned (B-scan) over the heart by using a galvanometer scanner. A second scanner was utilized to scan (C-scan) the beam along the other lateral direction, so that OCT data for a volume was obtained by stacking 300 cross-sectional images. An illustration of the scanning of the BZ in both the surface and transmural cases is shown in

Fig. 5.2. The rectangular boxes indicate the region that was scanned. in Fig. 5.2 (A), the fast scan (for cross sectional images) was performed from vertices 1 and 2 in the rectangular box and for Fig. 5.2 (B) vertices 3 and 4. Information in the 3D data set is presented by several cross-sectional (2D) images whose lateral locations are indicated on an en face image that is also obtained from the OCT data set. The en face image is calculated by integrating the cross-sectional images along the depth direction; therefore, its top-view-like image is derived from subsurface structures. A Canny edge detector was used to detect the top surface of the heart to reduce noise and undesired artifacts in the shallower range. The cross-sections were all stacked for a 3D visualization of the BZ using V3D software [77].

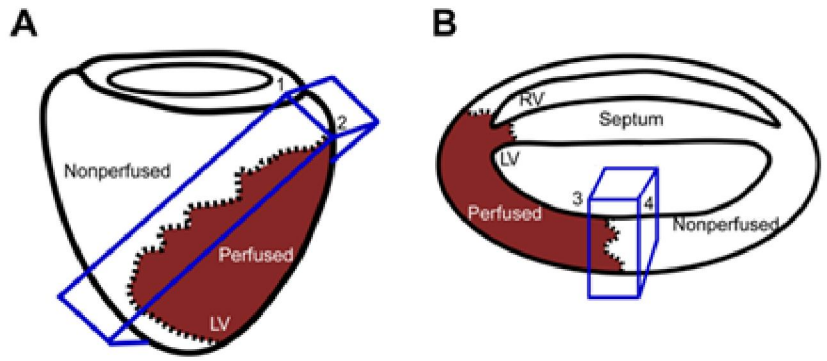

Figure 5.2. Schematic of the heart preparation for OCT imaging. (A) Longitudinal view of the BZ. For these scans, the heart was not sliced. The BZ is shown by the dotted line. The black rectangular boxes shows the region in which the 3D scan was performed. (B) The short-axis view of the imaged BZ.

5.4 Results

To examine the geometry of the BZ both epicardially and transmurally, we performed OCT scans on the epicardial surface of the heart before it was sectioned for transmural imaging. To perform

transmural OCT scans, we made two transverse slices (horizontal plane) through the heart to obtain a 3 mm thick slab of cardiac tissue; this slab was then imaged. Several cross-sectional OCT images were acquired from apex to base. Selected images from these scans are presented.

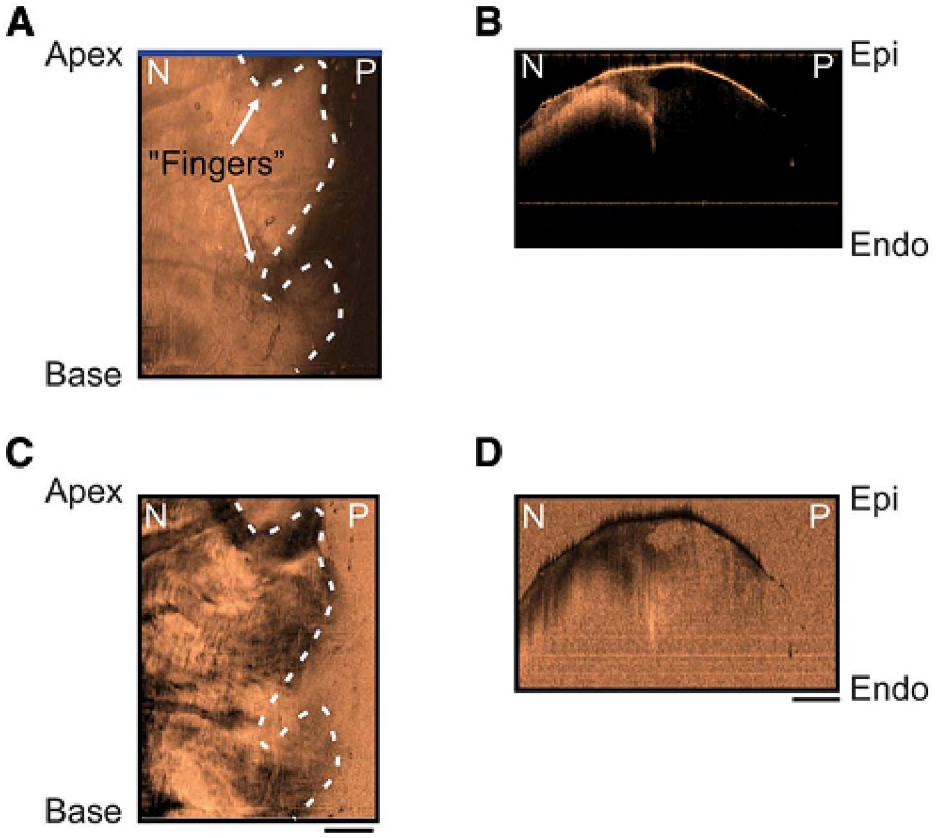

Figure 5.3. OCT 2D image of the BZ. (A) Reflectivity en face image generated by integrating the data along depth. Topological information as well as the BZ (white dotted line) can be seen. (B) OCT reflectivity image. Due to refractive index matching, the cleared region (right) is dark due to low backscatter, whereas the nonperfused tissue (left) is bright due to high scattering. (C) Retardance en face image. The dark region on the left is the nonperfused region, while the bright color indicates the perfused region. The BZ can be seen between the two regions (white dotted line). (D) OCT phase-retardance image. Imaging of the BZ transmurally showed "finger-like" projections of perfused tissue penetrating nonperfused tissue. P, perfused with BABB; N, nonperfused. Scale bar = 1 mm.

The OCT B-scans producing cross-sectional images were performed from epicardium to endocardium, simultaneously providing depth information from base to apex. Multiple cross-sectional images were acquired by scanning the beam along the perfused and nonperfused regions. Note that the C-scan in this configuration started approximately 2 mm to the left of the BZ and ended 2 mm into the perfused region, thereby capturing all of the BZ. Data from these scans are shown in Figs 5.5-8.

Figure 5.3 shows representative examples of reflectivity and retardance en face images (Figs. 5.3(A) and (C), respectively) and reflectivity and phase retardance cross-sectional OCT images (Figs. 5.3(B) and (D), respectively) of the epicardial surface of the cleared rabbit heart. In addition to the reflectivity, the form birefringence is also expected to reduce due to refractive index matching in the clearing process. The bright color in the reflectivity images (Fig. 5.3) indicates the nonperfused tissue that exhibits more scattering than the cleared tissue (black color). Because the nonperfused tissue is highly scattering, muscle fibers in this region can be seen; whereas in the perfused region, the refractive index is matched and fibers cannot be observed. Note that the reflectively en face image (Fig.5.3 (A)) displays anatomical information (i.e. vessels) and more importantly illustrates the complex structure of the BZ. In the retardance en face image (Fig.5.3(C)), areas of dark color indicate small birefringence, which might be reduced because of the clearing effect on birefringence. The area on the right includes noise caused by the SNR reduction due to refractive index matching in the perfused region. This could be seen in the reflectivity (dark color; Fig.5.3 (B)) and retardance (noise pattern; Fig.5.3 (D)) images. The

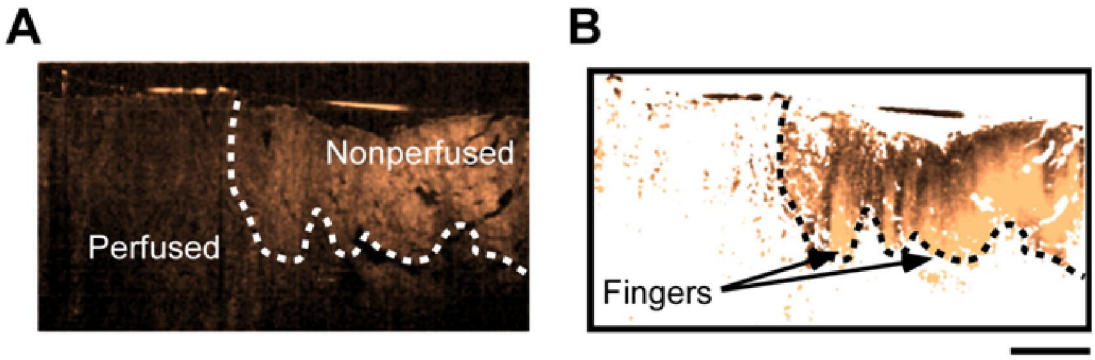

Figure 5.4. Demonstration of BZ in depth. The reflectivity (A) and masked retardance (B) image show the suggested BZ by a dashed line. Scale bar = 0.5 mm.

border between these two regions can be clearly distinguished (see BZ suggested by the white dotted line drawn manually in Figs.5.3 (A) and (C)). In the retardance images, the color change from dark to bright (epicardium to endocardium) represent higher birefringence typically in the nonperfused region. All the images demonstrate that the cleared tissue penetrates into the uncleared region in a so-called finger-like projection. Fig. 5.4 (A) and (B) show a potential BZ region in depth by the dotted lines. The delineation of the BZ is not as distinct in the reflectivity image (Fig. 5.4 (A)) as it is in the retardance image, Fig. 5.4 (B). The retardance image in this case is masked by the reflectivity image; this reveals the potential "fingers" of the BZ. Since shadowing effects can occur in OCT images and a decay of intensity in depth, using the depth direction for determining the BZ may not be the best approach and could lead to false positive or an observed BZ that is not an accurate representation of the true BZ.

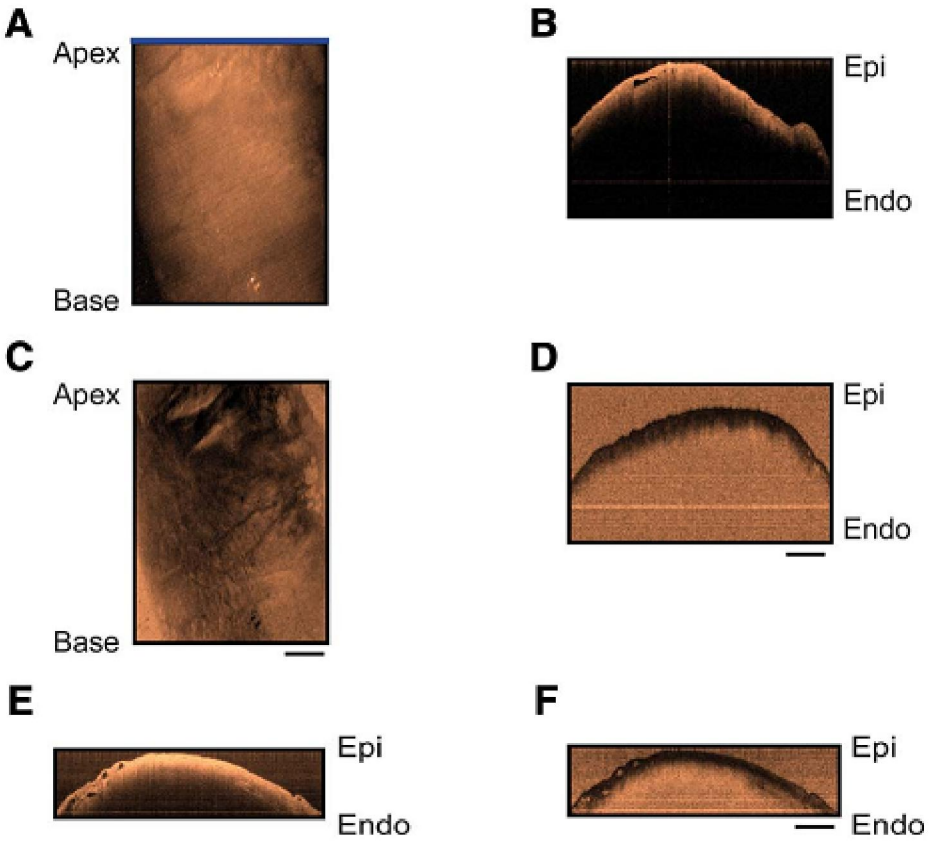

Figure 5.5. OCT 2D image of an uncleared heart. (A) Reflectivity en face image generated by integrating the data along depth. Topological information can be seen but there is no presence of a BZ. (B) OCT reflectivity image of uncleared tissue. No border can be observed. (C) Retardance en face image. The dark regions indicate that the tissue is nonperfused. (D) OCT phase retardance image. Only the epicardial surface can be seen due to the high level of scattering within the tissue. (E) OCT reflectivity image of the heart after treatment with ethanol. Ethanol does not significantly affect the penetration depth of light in the tissue as shown by the lack of border between the two regions. (F) OCT phase retardance image of the heart after treatment with ethanol. Only the epicardial surface is producing a signal due to low penetration depth within the tissue. Scale bar = 1 mm.

Fig. 5.5 depicts representative reflectivity and retardance en face images (Figs. 5.5(A) and (C), respectively) as well as 2D OCT reflectivity and phase retardance images (Figs. 5.5(B) and (D), respectively) of uncleared heart. These images are taken from the same area as in Fig. 5.3 just before clearing. Note that the heart was rotated slightly from Fig. 5.3 to capture more of the BZ.

The reflectivity and retardance en face images in Fig. 5.5 illustrate heart anatomy and explicitly show no signs of a BZ. In both Figs. 5.5(B) and (D), only the epicardial surface of the tissue can be observed due to the high level of light scattering and low level of light penetration in the tissue.

To determine whether the ethanol affects the penetration depth of the tissue during OCT imaging, we imaged the BZ after ethanol treatment. Representative 2D OCT reflectivity and phase retardance images are shown in Figs.5.5 (E) and (F), respectively. Note that only the epicardial surface of the heart is visualized in both OCT images, similar to Figs.5.5 (B) and (E). Therefore, the BZ that we observe in Fig. 5.3 is due to the difference in perfusion with the BABB solution and not due to any effects of the ethanol.

To determine if the "fingers" are present transmurally within the heart, we sliced the heart transversely, which is shown in Fig.5.6. Representative reflectivity and retardance en face images (Figs. 5.6(A) and (C), respectively) and 2D OCT reflectivity and phase retardance images (Figs. 5.6(B) and (D), respectively) of the cleared heart are depicted. The retardance image is noisy in the perfused region resulting from low reflectivity. Masking the retardance image with the reflectivity contrast (removing low reflectivity signal regions) can be used to aid in visualizing the retardance image. These images demonstrate a clearly distinguished border between the perfused and nonperfused regions of the heart (BZ suggested by the white dotted line drawn manually). Therefore, the BZ has a complex 3D geometry, both epicardial and transmurally, that is comprised of "fingers" of perfused tissue that protrude into the nonperfused region. It is worth noting that in the cross sectional images for the transmural case, demonstrated in Fig. 5.6 (B) and (D), is more consistent in depth with a higher contrast border that in the other dimensions imaged.

The cross-sectional OCT reflectivity and retardance images of the epicardial surface of the cleared heart at different locations are illustrated in Figs. 5.7(A) and (B), respectively. The image slices start on the apical surface (0.03 mm) and progress to the base (9.09 mm). The blue lines on the en face image denote where on the surface the slices were taken (Fig.5.7 (A)). The

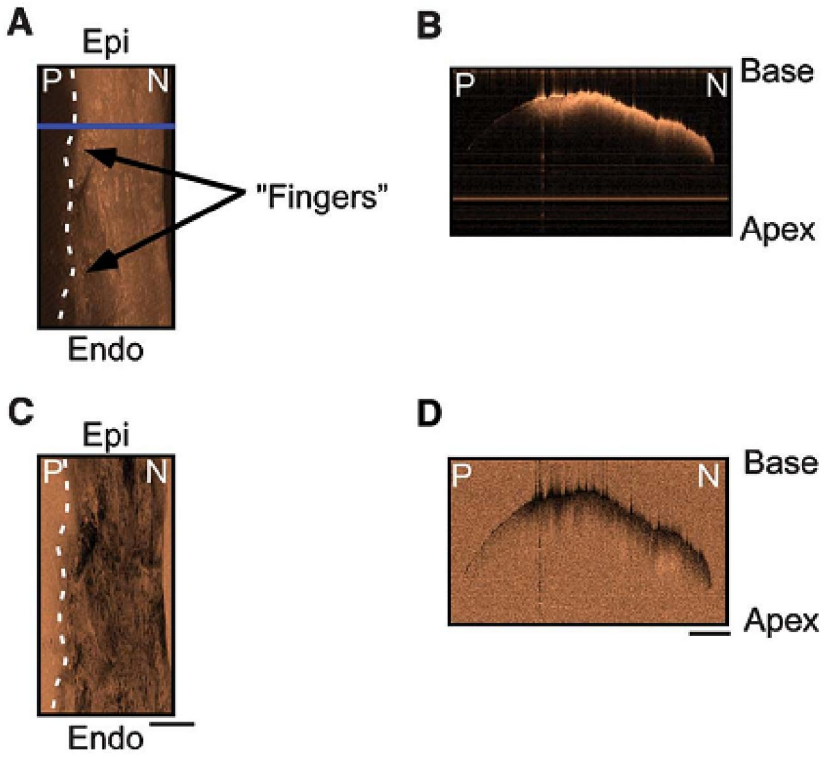

Figure 5.6. OCT image of the rabbit heart sliced transversely. (A) Reflectivity en face image generated by integrating the data along depth. Topological information as well as the BZ (white dotted line) can be seen. (B) OCT reflectivity image. Refractive index matching yields low backscattering in the cleared region (left), whereas the nonperfused tissue (right) is bright due to the high scattering. (C) Retardance en face image. The dark region on the right is the nonperfused region, while the bright color indicates the perfused region on the left. The BZ can be seen between the two regions (white dotted line). (D) OCT phase-retardance image. P, perfused with BABB; N, non-perfused. Scale bar = 1 mm.

nonperfused region is on the left, which can be seen due to the highly scattering nature of the tissue; the perfused region is on the right and can be seen through the depth due to the lack of scattering within the tissue. The "fingers" of the BZ can be clearly distinguished at each location through the tissue. For instance, there are distinct "fingers" on the apical surface (0.03 mm) and near the base (5.50 mm and 7.33 mm). However, the absence of visible "fingers" at 1.82 mm and 3.65 mm indicate that the number and size of the "fingers" change, supporting the complex 3D geometry of the BZ.

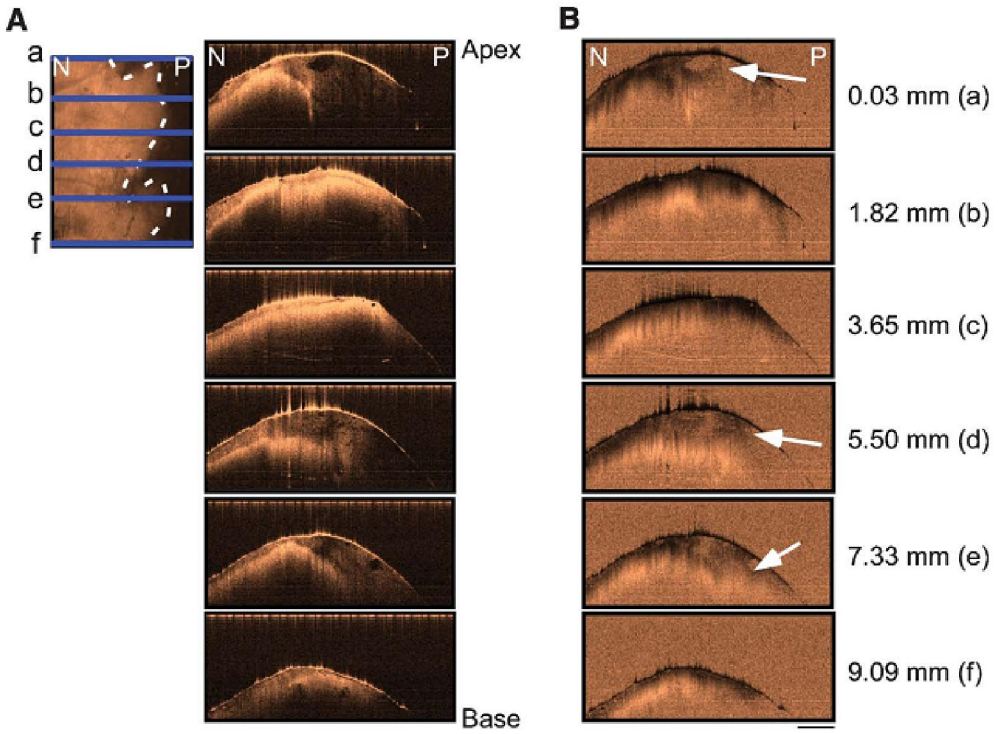

Figure 5.7. Snapshots of 2D OCT images of the perfused heart at different locations from apex to base. (A) Reflectivity. (B) Phase retardance. Slices start at the apex (0.03 mm) and progress to the base (9.09 mm). The reflectivity en face image shows where the slices were taken (as indicated by the blue line and letters). Arrows indicate "fingers." Scale bar = 1 mm.

To visualize the "fingers" of the BZ, we made a 3D reconstruction of the BZ using the reflectivity images. Fig. 5.8 shows that the perfused region is invisible because of the clearing, leaving the nonperfused region visible. The "fingers" of the BZ are readily observed.

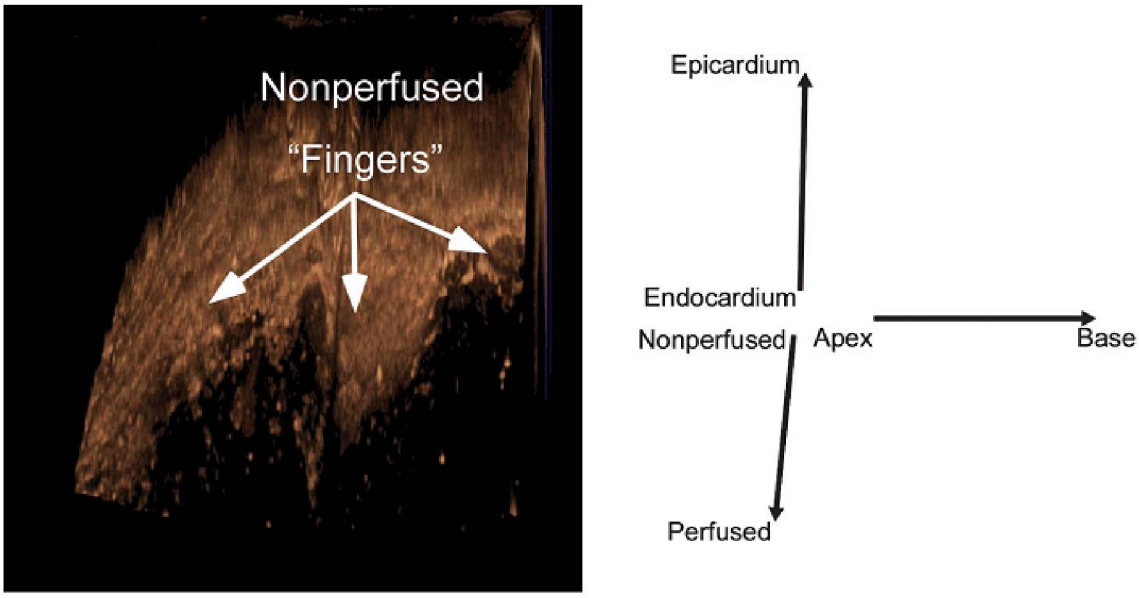

Figure 5.8. 3D reconstruction of the BZ from the reflectivity images. The bright region is nonperfused tissue. Areas of low-reflectivity signal indicate cleared tissue with low scattering. "Fingers" of the border can be easily seen.

5.5 Discussion

By using the combination of optical clearing and OCT, we were able to observe, with high resolution, the 3D geometry of the MI BZ of the rabbit heart with a15 μm axial resolution. In this manner, we have determined that the BZ is not a sharp transition between perfused and nonperfused tissue but is rather comprised of "fingers" of perfused tissue protruding into

nonperfused regions. The number and size of the "fingers" change both epicardially and transmurally, indicating a complex 3D geometry of the BZ.

In transparent tissue (via optical clearing), penetration depths of 3 mm can be expected. Even in uncleared cardiac tissue (up to 2 mm) [22, 78] OCT is still beneficial because the fibrous tissue and fat create an optical contrast within the myocardium. However, to image deeper internal structures of the heart using OCT (more than 3 mm), the tissue should be made transparent by using an appropriate clearing technique. For imaging studies, matching of the refractive index allows for imaging deeper within the tissue; this is due to a reduction in light scattering within the tissue. By adapting the optical clearing technique to create a BZ, we can see the border not only on the epicardial surface but also through the depth of the myocardium at a high resolution using OCT. It is important to note that the dark voids that we see in reflectivity en face images (Figs. 5.3(A), 5.5(A), and 5.7(A)) are most likely vessels, which may provide more information on how the tissue is perfused during MI experiments.

Form birefringence from the myocardial fibers was indicated by the retardance images in this chapter. When the heart was cleared, the refractive index difference between the short and long axis of the fibers was also reduced therefore not only reducing reflectivity, but the retardance as well. Further studies into the effects of clearing on birefringence could help elucidate how the optical properties are changed. Then by combining the contrast of reflectivity and retardance, perhaps by weighting the reflectivity image by retardance values, a greater SNR could result with a clearer image of the BZ geometry.

While electrophysiological changes at the BZ are a substrate for MI-induced arrhythmias, the 3D geometry may play a more important role in the initiation and maintenance of these arrhythmias. The geometry of the ischemic BZ was imaged with MRI and was found to be complex through the depth. When one perfusion region is made to be ischemic, it was found that the irregular geometry formed transmural pathways leading to fast reentry, facilitating and maintaining the ventricular arrhythmia. Therefore, it is imperative to determine the 3D geometry of the perfusion BZ in order to understand arrhythmogenesis during MI, which could be done in future studies. Further studies are necessary to correlate the BZ geometry with its respective electrophysiological properties.

5.6 Conclusion

In summary, our technique capitalizes on the properties of the optical clearing process and depth-resolved PS OCT to nondestructively image the BZ with a high spatial resolution. Furthermore, this imaging process will help characterize the electrophysiological consequences of MI that lead to fatal arrhythmias by correlating BZ geometry with arrhythmogenic reentry.

Chapter 6

Imaging The Salamander Retina

6.1 Overview

Applying OCT to measure neural function has been demonstrated on a variety of samples, including the retina. These signals are very small and susceptible to noise from the retina itself or environmental effects. With the high resolution of OCT images, very small motion artifact can result in observing a different location on the sample, confounding the measurement or producing erroneous results. Reducing these artifacts, stabilizing the sample and performing signal processing to observe a consistent signal is challenging. In this chapter, the salamander retina is imaged both structurally and functionally. Structural images of the retina are presented demonstrating images from several retinal layers as well as high resolution images resolving the photoreceptor mosaic and clearly delineated layers. Functional OCT signals, what they can measure, and how they relate to the retina will also be discussed. The photoreceptor layer demonstrates the strongest indicator of function and the physiologic mechanism of the observed signals are also discussed. Signal processing is also presented to stabilize the sample and reduce noise in the measurement.

6.2 The Structure of the Retina

The retina is a layered tissue at the back of the eye ~250 μm thick that transduces visible light into electrical signals which are sent into the brain. An OCT image of the salamander retina is

shown in Fig. 6.1 showing all the layers. The layer between the retina and the sclera (outer layer of the eye) is the choroid. It is the vascular layer of the retina providing oxygen and nourishment to the retinal layers. The choroid also contains connective tissue as its location is at the border between the retina and sclera. Connected to the choroid is the retinal pigment epithelium (RPE). Attached to the outer segment of the photoreceptors, the RPE provides nourishment to the photoreceptors, aids in buffering ions used during visual transduction and absorbs light not absorbed by the photoreceptors to improve the image quality of the retina. The major type of supporting glial cells in the retina are known as Müller cells and traverse the entire retina. The

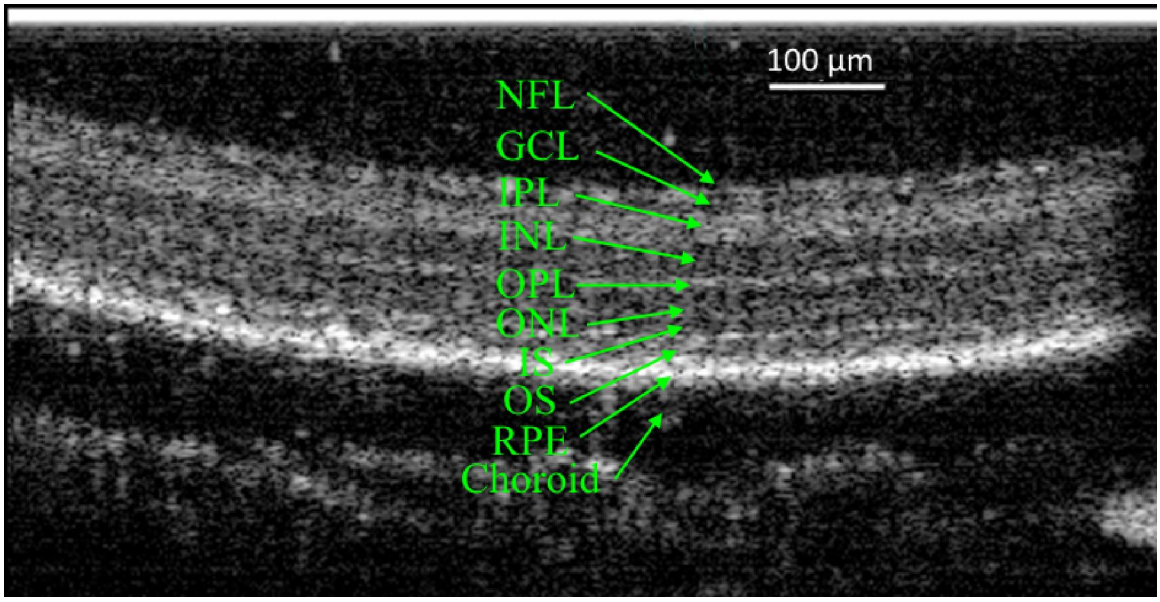

Figure 6.1. Cross section of a salamander retina from an eyecup preparation taken with a high resolution SD OCT sytem at center wavelength of 905 nm. The layers of the retina are labeled in green. NFL, nerve fiber layer; GCL, ganglion cell layer; IPL, inner plexiform layer; INL, inner nuclear layer, OPL, outer plexiform layer; ONL, outer nuclear layer; IS, inner segment of photoreceptor; OS, outer segment of photoreceptor; RPE, retinal pigment epithelium.

functions of Müller cells include aiding in regulating potassium, neural transmitter uptake and mechanical support of the retina.

The first site of visual transduction occurs at the outer segments of the photoreceptors. As light first enters the retina, it passes through all of the retinal layers before being absorbed by the photoreceptors. The inner segment of the photoreceptors is filled with mitochondria supplying the demanding energy requirements for the membranes proteins of the outer segment as well as increasing the refractive index of the cell [79]. A higher refractive index acts as a waveguide for the photoreceptor which inhibits stray light noise [80]. A more in-depth treatment of the chemical signals and their respective scattering properties in the outer segment will be discussed in the next section. The cell bodies of the photoreceptors make up the outer nuclear layer while the axons terminate in the outer plexiform layer on bipolar cells. The bipolar cell layer receives input from one to several photoreceptors (rods or cones, not both) and transmits that information to the ganglion cell layer. Bipolar cells are described as being either ON or OFF in their response to light and their cell bodies are located in the inner nuclear layer. Bipolar cells are also connected to interneurons, horizontal and amacrine cells. In addition to having synapses on bipolar cells, horizontal and amacrine cells integrate information from the photoreceptors and ganglion cells, respectively. Lastly, retinal ganglion cells make up the ganglion cell layer and their axons form the nerve fiber layer. The graded signals received from bipolar cells and interneurons are converted to action potentials which are sent to the brain via ganglion cell axons. All of the nerve fibers exit the eye at the optic disc, shown in the OCT cross section in Fig.6.2 below.

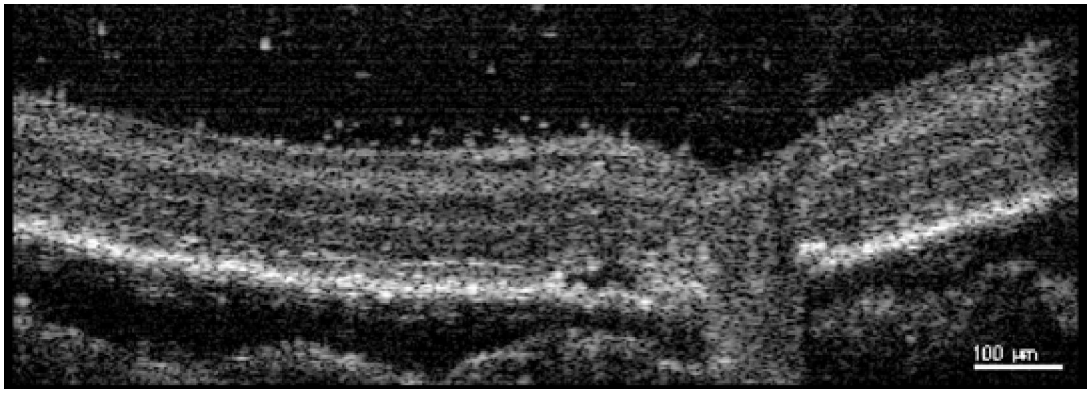

Figure 6.2. Cross section of salamander retina taken with a high resolution SD OCT system at center wavelength of 905 nm. The optic disc can be observed as a break in the retinal layers.

6.3 Visual Transduction

As the chemical messengers involved in phototransduction were being identified, their kinetics and stoichiometric relationships were also investigated. Most of the results presented here will be from amphibian retina in the NIR range as it is most relevant to the OCT systems that were used for measuring retinal structure and function. When looking for functional signals in the retina, the imaging wavelength is very important. If the wavelength is too short, such as ultraviolet light, the retina could be damaged while visible light will activate the photoreceptors. If the light used for assessing function has too long of a wavelength, the amount of measured backscattered light will be reduced due to an increase in the mean-free path length and water absorption. An increase in water absorption described in terms of the attenuation coefficient is a decrease in the scattering coefficient and an increase in the absorption coefficient. This is most likely the primary contributor to the small signal from the 1300 nm based system. From simulation of the bovine

retina [81], at 633 nm, the mean-free path is calculated to be 1 mm [82] and is already one and a half times that at 1050 nm.

As mentioned above, when photons enter the retina, the first site of phototransduction is at the outer segment of the photoreceptors. Photons activate rhodopsin (Rh*), a light-sensitive protein that is the main pigment in rod photoreceptors, on the outer segment discs which stimulates transducin. Transducin is a G protein that has a large role in phototransduction such as leading to conformation changes in rhodopsin and activating phosphodiesterase. The interaction between Rh* and transducin exchanges transducin's bound GDP for GTP expelling its β and γ subunits. The remaining α subunit and GTP (referred to as G*) then activates phosphodiesterase, converting cyclic-GMP (cGMP) to GMP. This reduces cGMP concentrations which are gating the ionic channels on the photoreceptor membrane and therefore cause the membrane ion channels to close, decreasing Na^+ currents. There are several measurable optical properties of the photoreceptor that change during phototransduction that are indicators of function.

6.4 Intrinsic Optical Signals

Once the primary contributors of the possible relative intensity and swelling/refractive index changes are identified, analysis of OCT datasets can be directed to look for the most likely signals to produce repeatable indicators of function. One of the earliest time-series measurements of NIR scattering during retinal activation was done by Hoffman [83] in rod outer segment suspensions. These signals were also discovered by Harary [84]. Classification of these signals were investigated by Kühn [85] identifying activated rhodopsin binding transducin, called the binding

signal, also measured in rod outer segment suspensions. Measurements for scattering changes are usually represented as a relative intensity change by the following equation

$$\frac{\Delta I}{I} = \frac{I - \bar{I}_{pre}}{\bar{I}_{pre}} \qquad \textbf{6.1}$$

Where I_{pre} is the mean of the pre-stimulus signal and I is the intensity of the signal. The sign for the relative change in intensity for the binding signal for a light scattering was positive. The dissociation signal, after dissociating from activated rhodopsin resulted in a signal opposite in sign but greater in magnitude since each step in the phototransduction cascade is amplified, each step's magnitude increases exponentially. Each step in the phototransduction cascade has alternating positive and negative deflections which is expected from scattering theory [86] due to changes in molecular size from binding and unbinding processes. The previous studies were, however, carried out in suspensions in un-physiologic proportions [87]. PDE activation was found to be a measurable signal from NIR scattering from intact retinas [88]. It is worth noting that ionic currents (perfusion with low [Na^+]) were not significant contributors to this signal and the net result suggests the PDE signals to be the primary source of NIR scattering in the photoreceptors for an in-tact retina [89].

Indirect effects of signal transmission in the retina, such as changes in cellular swelling, birefringence [90] and index of refraction (results in change of optical path length) [91] are also present in the photoreceptors as well as other layers. Given the specifications of an OCT system, however, index changes (1-2% for complete bleaching) result in optical path length changes of ~2 nm (assuming no significant changes in physical dimensions) which are just at or above the noise floor for phase signals (0.5 - 2 nm as measured in Chapter 2). Thickness changes (swelling)

of the photoreceptor could be observable with cross sectional scanning in the appropriate location but for sub-bleaching stimuli it hasn't been consistently measured from OCT. It has been measured consistently, however, from NIR imaging with signal processing [92]. Changes in birefringence are also below threshold and are measured perpendicular to the photoreceptor which may have a significant form birefringence component. Birefringence results are also from fixing retinal tissue that has been bleached which may not be detectable from functional imaging and non-bleaching stimuli. Standard OCT imaging beam is oriented parallel to the photoreceptor. Finally, vesicular release and calcium signals have only been measured with fluorescent probes [93] and consistent measurements of intrinsic optical scattering or absorption changes during activation have not been reported.

Since graded potentials are used from the rods to the bipolar cells, the IOS from them may not be the same as from brain slices or nerves. Illumination of the entire retina and recording at the optic disc with NIR imaging has produced repeatable signals [94]. Swelling and birefringence changes from squid giant axons (imaging beam normal to the photoreceptors) are possible but not likely in vivo in the retina due to the orientation of the processes of the plexiform layers. Amacrine and horizontal cells are oriented normal to the imaging beam and could produce a signal if they are dense enough among the bipolar axons. Ganglion cell axons could also produce a signal if the entire retina is stimulated as mentioned above since the relationship of inner retina activity to nerve fiber layer activation are not known at the time of experiment and would be difficult to identify for a spot stimulus.

6.5 IOS Sources for general nerve activation

Since the seminal work of Cohen in the late 60s [95], light scattering signals have been thoroughly investigated during neural activation. Due to the large diameter and slower signal transmission of non-mylenated axons, their optical changes during neural activity can be more closely investigated than very small bundles of myelinated axons. Foust and Rector [96] have isolated the scattering and birefringence responses for non-myelinated lobster walking leg nerves by using voltage sensitive dyes and various drug interventions to vary swelling, refractive index and membrane potential. It was found that birefringence signals were quite large compared to scattering signals and followed the membrane voltage closely in shape and time course. This was verified further with voltage sensitive dyes. 90° light scattering signals, which are hypothesized to result from change in interstitial spaces, were altered when agents were applied to the nerve that changed cellular swelling and refractive index. Studies of scattering changes of cell cultures and brain slices determined that changes in refractive index resulting from changes in cell volume were the primary contributor to the measured signals [97-100]. Functional OCT signals have also measured transient thickness changes during activation by using the phase information [1] as well as reflectivity measurements with voltage sensitive dyes [101]. All of the studies mentioned here have the incident beam normal to the surface of the axons. Since the orientation of the axons in the retina are parallel to the beam (except for horizontal and amacrine cells), this may affect the ability to obtain a signal based on cellular swelling or index changes.

The electroretinogram (ERG) is a common measure of retinal activity. It measures the radial extracellular currents from the retina during activation. The ERG is measured from an electrode placed in the eyecup and the reference electrode placed behind the eyecup. An ERG waveform is

shown in Fig. 6.4 with the functional OCT signals. The fast downward deflection is called the a-wave and represents the activity in the photoreceptor layer. The main component of the ERG is after the a-wave, the b-wave, and it represents all activity post-synaptic to the photoreceptors. The ERG is used as a marker for the time course of retinal activity but since the inner retinal layers communicate with graded potentials, observing an optical signal as the result of ionic currents may not be possible. As mentioned earlier, when the retina is perfused with a solution with low Na^+ concentration, the electrical response is all but removed yet the NIR scattering signal in photoreceptors remain [88]. Our approach to observing scattering signals in the retina will therefore focus on the outer segments of the photoreceptors.

6.6 Functional OCT signals and interpretation

6.6.1 Understanding OCT measurements

The OCT signals that will be discussed in this section are reflectivity and phase. The reflectivity signal is the standard OCT contrast and represents the intensity of backscattered light from a sample and is based on the magnitude of the complex depth profile for SD OCT. The phase signal is the phase component of the complex depth profile and as mentioned in Chapter 2, represents a small nanometer-range optical path length changes of a sample. Changes in reflectivity and phase can indicate different phenomena and both will need to be compared and contrasted to understand what phenomena is being measured from a sample. Changes in the reflectivity signal can reflect more than a change in backscattered intensity as it will shift the depth profile up and down. Movement of the sample can also be observed as changes in reflectivity. For large movements, a switch in sign in consecutive depths will be observed that can complicate interpretation of results.

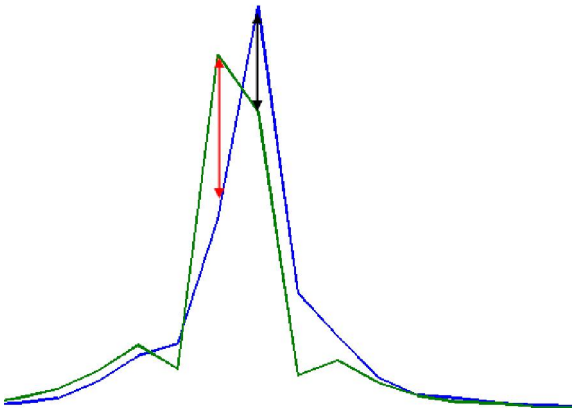

Figure 6.3. Two coherence functions demonstrating the effect of reflector motion that couples into reflectivity. The red line shows the negative signal change from the green coherence function to the blue and the black line demonstrates a positive change from the green to blue coherence function.

This is shown in Fig. 6.3. Being depth-resolved, deeper regions can be affected by reflectivity changes in shallower regions resulting in a shadow effect. This could also give false positives for an observed signal. Changes in the phase signal are usually indicative of small movements inducing optical path length changes of a depth location. The movement will also couple to the intensity signal as shown in Fig. 6.3.

To observe small phase changes and reduce potential coupling to the reflectivity signal, several approaches can be used. A reference surface, such as a piece of glass above the sample, will provide a reference phase, which will have common noise and trends of the sample due to environmental effects on the entire system. Therefore, these artifacts can be removed from the measurement by subtracting the reference phase from the sample phase. If no reference surface is available, global motion of the sample can be corrected by averaging the phase from the depth locations with the highest SNR and then compensating the depth profile using the translation property of the Fourier transform. Compensation is done by multiplying the spectra by a complex

exponential, *exp(-i*k*z),* where k is the vector of wavenumber values for the spectra and z is the path length to adjust the depth profile. After obtaining the time-varying path length change, this calculation is performed on the interpolated spectra, prior to applying the FFT operation to obtain the stabilized depth profile. This method will then correct for common phase-induced changes in the reflectivity signal. It is possible, however, that if the depth points used to stabilize the retina have signal themselves, that signal could be induced to all other locations, resulting in false positives. Since OCT is high resolution swelling is a potential signal that is investigated, care must be taken in correcting cross sections with other motion correction algorithms as well.

6.6.2 Possible OCT Signals in the Retina

To determine what signals will be closely inspected and what may be possible imaging with OCT, the IOS sources previously mentioned with the OCT signals will be discussed to get an idea of what will be measureable.

Visual Transduction

The major contributor to scattered signals in the NIR range in phototransduction is the phosphodiesterase signal [89]. This produces a positive deflection for scattering measurements and is a verified signal from scattering experiments. These changes would be observed from the reflectivity signal and the relative measurement ($\Delta I/I$) should provide an indicator of function. The phosphodiesterase signal should not change optical path length or position of the photoreceptor so no phase signal is to be expected.

Changes in Birefringence and Refractive Index

With a bleaching stimulus, birefringence and refractive index have been measured in photoreceptors [90, 91]. The numbers reported, however, are below the noise threshold for SD OCT, even with reference subtraction and phase compensation for global motion mentioned above. For other retinal layers a measurable signal may be possible, since birefringence is shown for activation for an incident beam normal to the axon. A change in index would be observed as a small movement in the phase signal and the reflectivity signal could also change depending on the index difference between the two layers being measured.

Swelling

Swelling of retinal layers during activation has been proposed and suggested as a cause for changes in $\Delta I/I$ but it has only been reported in squid retina [102]. If swelling is measurable with OCT, the phase signal would reflect it. If the swelling is large, it will also couple to the reflectivity signal. It is also possible that swelling could change the reflectivity signal due to a change in interstitial spaces. Depending on the location of the depth point and its location on the coherence function, these two reflectivity signals could combine constructively or destructively.

Depolarization

Ionic currents are responsible for swelling changes during neural activation but are an indirect measure. Only birefringence has been reported to closely match both the time course and morphology of the membrane potential. This has not been reported in retinal layers but could be investigated with a PS OCT system.

6.7 Functional OCT Signals Measured From the Retina

The feasibility of measuring changes in relative intensity during photonic stimulation of the retina using OCT has proven to be possible [2, 6] with an average of 10 or 100 scans in isolated retina. Positive changes were detected in the outer segments of the photoreceptors which is expected from previous observations of NIR scattered light during activation. Although there is a significant difference reported in the intensity signal resulting from stimulation, the response has not shown to produce a repeatable morphology. Muller cells go entire length of retina terminating at cell body or inner segment of photoreceptor and can get in the way of functional imaging blocking any signal [2]. Functional imaging with flood-illumination NIR microscopes measuring turbidity [103, 104] has demonstrated a morphology similar to the transient changes previously measured during phototransduction [88]. However, transmission measurements are not possible for clinical use and so more robust imaging and/or processing methods need to be implemented for OCT measurements that could potentially provide clinic utility. Intrinsic changes have been measured *in vivo* in chicken [3], macaque monkeys [5] and in humans [4] using OCT although the imaging procedure for human measurements was very tedious and required many trials. The imaging beam on the sample is mostly ~10 μm for the OCT studies and so M-mode measurements are susceptible to small movements of the retina that could significantly change the location being imaged. To address this, functional OCT measurements have been observed using *en face* [105] and B-scan images [3]. Our OCT imaging system allows for directed scanning for determining regions of high SNR and records time series measurements of retinal volumes. Phase adjustment methods were also used to reduce phase signals from cross-coupling

to the relative intensity measurements. An in-depth discussion of functional OCT signals related to electrical/optical/physical phenomena is provided in the next section.

6.8 Retinal Preparations

For functional experiments, eyecups were prepared from larval tiger salamanders (ambystoma tigrinum from Charles D. Sullivan, Nashville, TN) in accordance with approved IACUC protocol. Dissection was performed in low-light conditions. First salamanders were decapitated and pithed then the eye was enucleated. The cornea, iris and lens were then removed as well as the vitreous humor under a dissection microscope. The retina remained intact with the RPE and after dissection the eyecup was perfused with an oxygenated amphibian Ringer solution containing 110 NaCl, 2.5 KCl, 1.8 $CaCl_2$, 1.0 $MgCl_2$, 10 Hepes and 5 D-glucose in mM (pH 7.8) [106] and allowed to recover for 15-20 minutes. The Ringer was kept at 16° C with a Peltier cooler and the flow rate was constant at ~2 mL/min. A chamber for housing the retina during the experiment

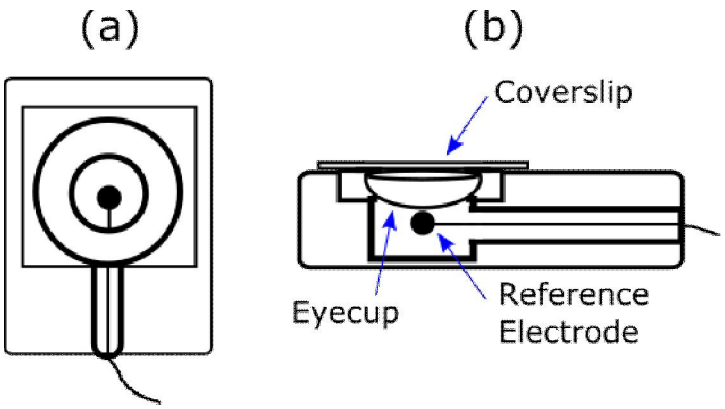

Figure 6.4. Diagram of perfusion chamber for retina experiments. (a) is top view and (b) is side view.

is shown in Fig. 6.4. To maintain a good connection with the reference electrode, cotton was placed under the eyecup and rested on the reference electrode. Before and after experiments, an ERG was recorded to assess the viability of the retina using Ag/AgCl glass electrodes with pulled tips of ~700 μm. ERGs recorded are shown with the OCT results in the next section. Prior to functional recordings, a structural 3D image was taken to provide a reference to all recording locations as well as provide structural information of the retina. For the functional measurements, a glass coverslip was placed on top of the retina to eliminate water evaporation and provide a reference surface for phase measurements. Several silent perfusion configurations were applied but the phase noise measured was still considerable. Therefore, perfusion was not performed during the recordings due to the noise introduced by perfusion.

6.9 Functional Experiments

6.9.1 Stimulus

Once a 3D volume was acquired, locations were chosen for stimulation and recording. The stimulus was a white LED (Rebel Neutral White, Luxeon, Ontario, Canada). The spectrum for the stimulus was recorded with a commercial spectrometer (CCS200, ThorLabs, Newton, NJ) and is displayed in Fig. 6.5. This was done to calibrate the stimulus intensity with a photoreceiver to produce a stimulus that will not bleach the retina but still provide sufficient stimulation. The stimulus went through several optical components that affected its spectrum which is why the

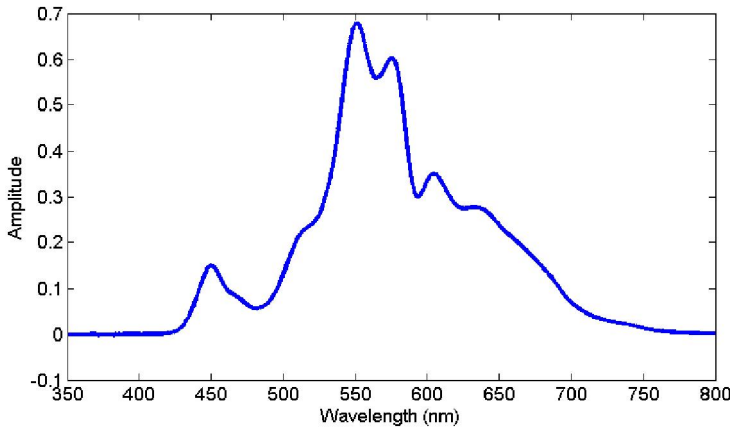

Figure 6.5. The spectrum of the light stimulus.

spectrum provided in the datasheet was not used. After the sample optics, the stimulus spot on the sample had a radius of ~75 μm^2 and an intensity was set at 3e-11 W/μm^2. At each location, five trials were recorded with a pre-stimulus period of 1 second followed by a 50 ms light pulse. There was three minutes between trials to allow for recovery of the retina and five trials with no stimulus recorded for a control. Each subsequent recording location was positioned at least 500 µm from the previous site.Each functional scan spanned an area of 80 µm x 40 µm in order to record from multiple photoreceptors. The *ΔI/I* response was averaged over the photoreceptor layer approximately 8 µm in depth, 56 µm in the x direction and 40 µm in the y direction. Only a part of the x direction scan was used due to artifact from the galvo turning point during fast 3D scanning.

6.9.2 SD OCT System configuration for functional imaging

The SD OCT system used for retinal imaging was PMF-based PS system using a line scan camera (sprint 140k, Basler, Ahrensburg, Germany) for detection and is shown in Fig 6.6. The source had

a center wavelength of 840 nm with a 50 nm bandwidth. In the reference and sample arm, a telescope is used to increase the beam diameter to fill the aperture of the water immersion lens (Objective W N-Achroplan 10x/0.3 Carl Zeiss, Oberkochen, Germany) to enhance the lateral resolution. The telescope in the reference arm compensates for optical dispersion in the sample arm which will then only require less compensation in software, producing for reliable depth information. The decay of single reflectors from a wedge prism with no telescope in the reference arm resulted in a nonlinear profile, which is not representative of the raw data measured. Experiments were also executed on another system with similar configuration, but it operated at 1300 nm wavelength region with a large bandwidth of 200 nm.

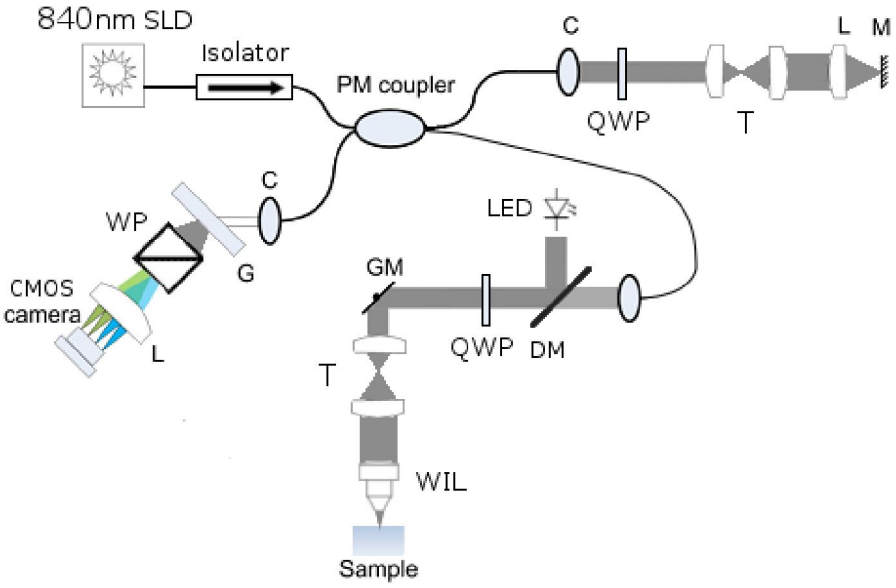

Figure 6.6. Schematic of SD OCT system for retinal imaging. SLD, superluminescent diode; C, collimator; QWP, quarter-wave plate; L, lens; M, mirror; LED, light emitting diode; DM, dichroic mirror; GM, galvo mirror; T, telescope; WIL:, water immersion lens; G, grating; WP, Wollaston prism.

6.9.3 Structural Imaging

En face imaging of retinal layers has been reported in humans [107] but not in the salamander. En face images of the retina are shown in Fig. 6.7. The layers of the retina were not entirely clear for the ganglion cell layer and the photoreceptor layer making automated edge detection very difficult for creating smooth en face images from these layers. The horizontal artifact present in Fig. 6.7 (b) and (c) is a result from manually selecting the layers for all 300 cross sections. The optic nerve head is visible in Fig. 6.7 (a) as the dark circle in the middle part of the retina image and in (b) where the nerve fiber tracts are directed to. The photoreceptor layer of Fig. 6.7 (c) is able to resolve some photoreceptors but the mosaic is not very apparent. However, focusing the light on a particular layer could enhance the imaging results from that layer.

6.9.4 Functional Results

An example of the locations imaged during an experiment is demonstrated in Fig. 6.8 on an en face image of the photoreceptor layer. The red boxes are the locations of functional recordings. A demonstration of the phase correction for global motion is shown in Fig. 6.9. The uncorrected phase signals are suggesting that the sample was drifting in the axial direction. After correction, the phase signals appear to be "detrended". This could help reveal phase signals that were masked by the low frequency motion. Unfortunately, phase signals from the retina were not observed with either OCT system and phase noise was greater than expected phase signals for the photoreceptor

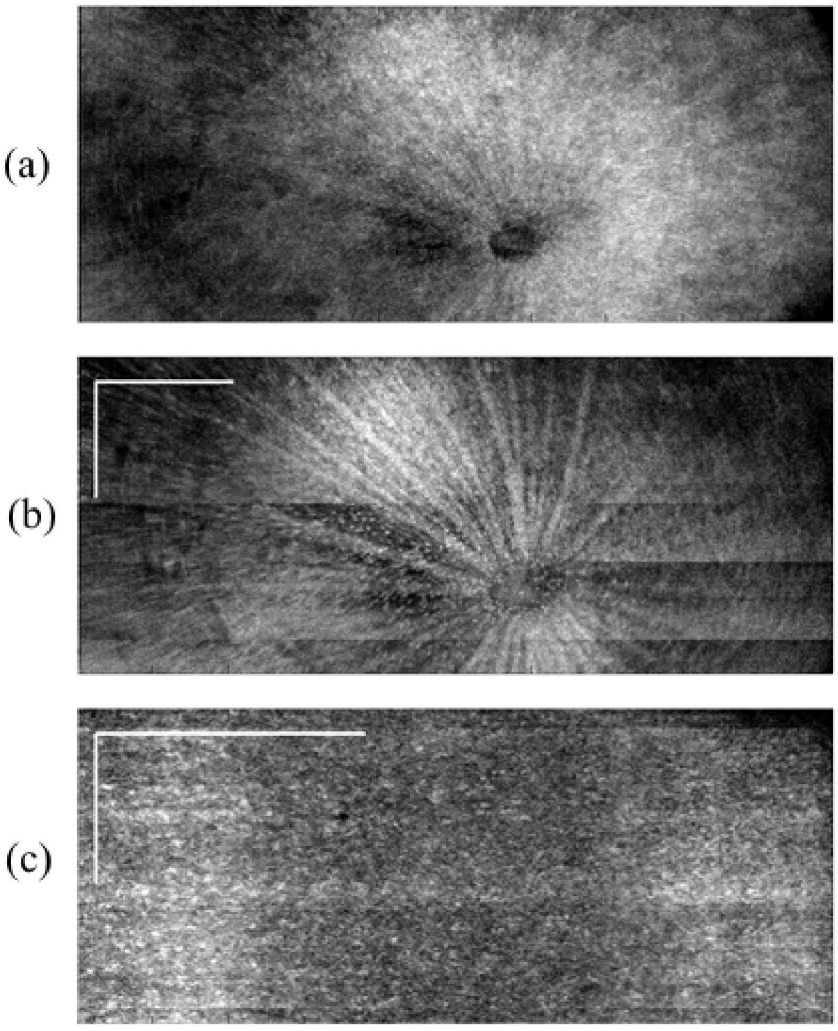

Figure 6.7. En face images of salamander retina with (a) integration of all the retinal layers, (b) integration of only the nerve fiber layer and (c) integration of the photoreceptor layer. Scale bars: 250 μm.

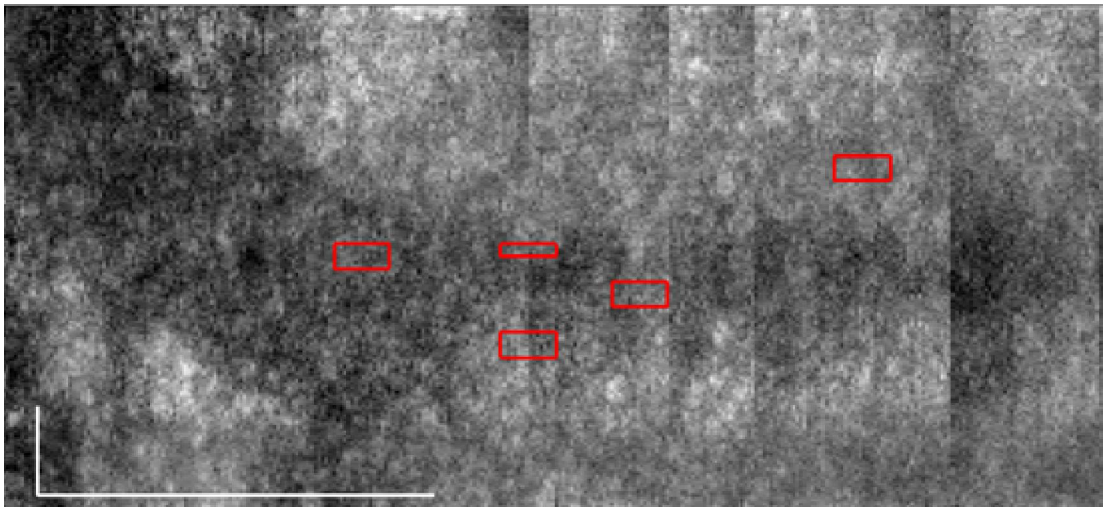

Figure 6.8. Image of retina with locations imaged highlighted by red boxes. Scale bars: 250 µm.

layer. A reference glass was used for the retinal recordings but due to the depth difference between the surface of the glass and the retina, they were not in comparable imaging ranges.

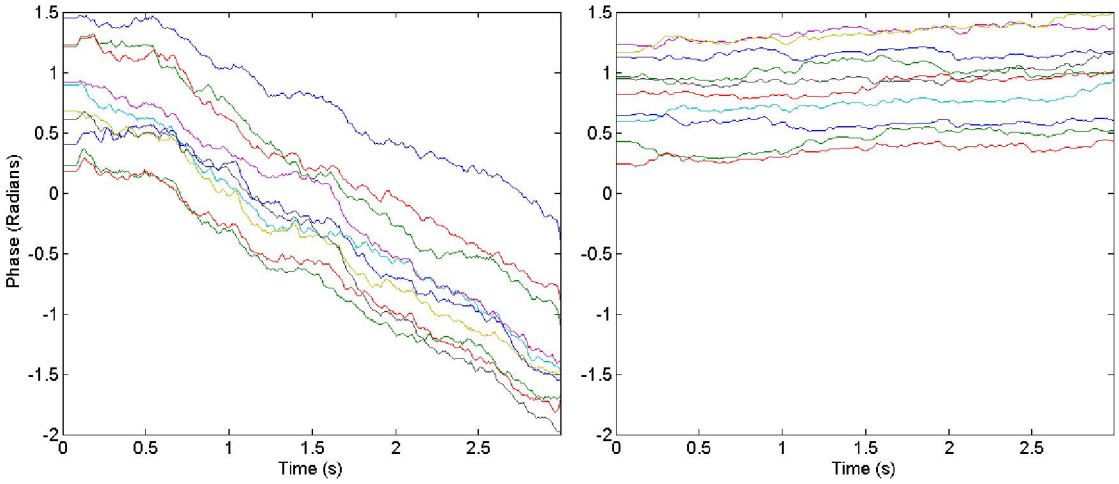

Figure 6.9. Example of phase adjustments to stabilize the sample image axially. (left) uncorrected phase for several depth locations and (right) the adjusted phase signals.

Reference subtraction from stable reflectors in the retina was also attempted, yielding no discernible signal.

Fig. 6.10 demonstrates the effect of phase adjustments on *ΔI/I* response. The noise level was reduced by ~12%. The 1300 system had an overall weaker reflectivity signal and fewer locations were observed to have signal. It is important to note that the phase signals that were used to compensate the signal in Fig. 6.10 did not appear to contain any signal. There is no evidence suggesting signal was induced or suppressed by the phase correction operation. From observing the adjusted and not adjusted signals, no new morphology appears to be introduced other than a reduction in the noise level.

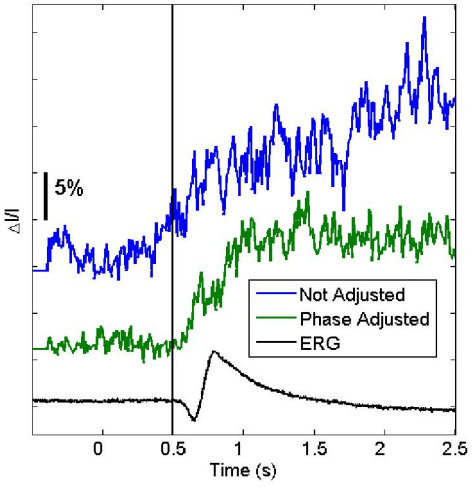

Figure 6.10. Effect of phase adjustments on a detected *ΔI/I* signal for the SD 1300 nm system for a single trial (averaged spatially). The vertical black line indicates the time of the stimulus.

(A)

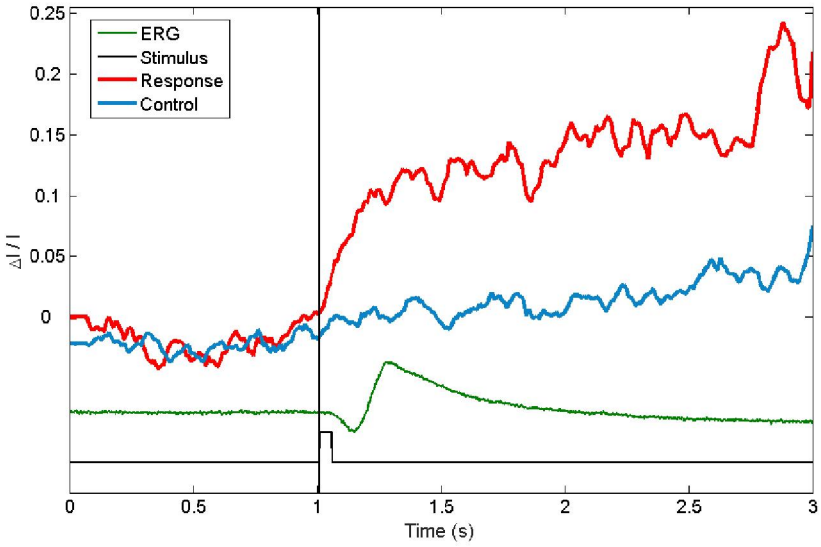

(B)

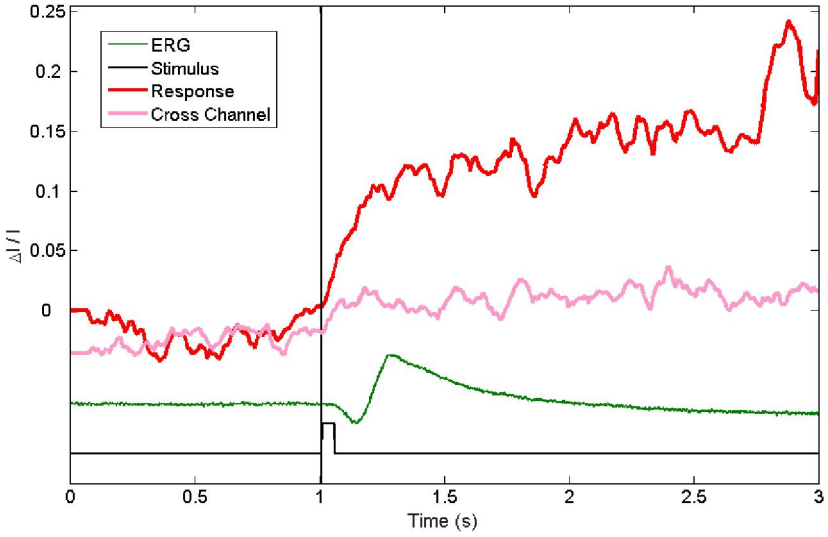

Figure 6.11. Response from 840 nm system for a single trial (average spatially). The vertical black line is an indicator of the stimulus onset. (A) demonstrates a response with a control signal from the main channel; while (B) includes the result with the cross channel.

In Fig. 6.11, a response from the SD 840 nm system is shown. The signal coincides with the start of the stimulus and is from a single trial. The rise in the response does not appear to track the a-wave of the ERG. Both the control and response signal (Fig. 6.11 (A)) were after the phase signal

was adjusted to reduce noise. It is important to note that subsequent trials at a single location were not as strong as the first trial. This suggests the power of the light stimulus was set too high and/or enough time wasn't given between trials to allow the retina to completely recover. In panel (B), the cross channel from the PS SD OCT system is also shown. The cross channel only demonstrated significant intensity in the RPE layer, which is known to be polarization scrambling. Any change during functional activation, however, is very small with a low SNR. In all experiments, no significant cross channel signals were observed in the retinal layers.

Chapter 7

Conclusion and Outlook

7.1 Conclusion

Several aspects of OCT systems from hardware to software have been improved upon in this work. I've demonstrated system configurations to increase throughput and real-time processing and systems to increase SNR while removing common noise. Real-time processing of OCT data with a constant throughput of 700 MB/s upwards of 1.1 GB/s is possible without compromising bit depth, imaging depth, or image quality. A phase unwrapping algorithm was implemented for an PS SS OCT system on an FPGA. In addition to real-time processing, synchronized OCT systems were realized to send control signals, record analog signals and even acquire from a second OCT system; all based on the same clock.

A balanced detection system was also demonstrated that doubled the measured OCT signal (increase of 6 dB) while reducing common noise terms, such as DC and auto-interference by 12-18 dB with no software enhancements. The carefully aligned spectra were imaged on an area camera which provided identical wavelength mapping that was capable of maintaining signal gains from balanced detection in depth, up to at least 2.64 mm. The system also has a high sensitivity for SD OCT at 106 dB.

Biological samples were also investigated to observe structure and function. The border zone for isolated rabbits hearts was nondestructively imaged in 3D, uncovering interdigitations at a micro-

scale to aid in understanding how the border zone geometry relates to post-infarct fatal arrhythmias. The border zone was observed in both lateral and transmural direction. Reflectivity and retardance images provided two aspects of the border zone that had significant overlap.

The salamander retina was imaged displaying the photoreceptor mosaic and nerve fiber layer with a water immersion objective. Most of the layers of the retina were resolvable and these images were used as a guide to functionally image the photoreceptor layer of the salamander retina. The retina was functionally imaged using a directed scanner to track all imaged locations and simplify searching for recording sites. Phase stabilization of the sample was executed to remove drift in the phase signal and reduce noise in the reflectivity signals by 10-20%. Although these processing methods proved useful and single trial measurements are possible, the frequency and repeatability of measurable responses to light stimulus were not significantly greater than those reported in literature.

7.2 Outlook

FPGAs continue to grow in their complexity with 3D chips now available. This is important due to the major limitation of FPGAs being routing. A complex algorithm will need a lot of space and might not route correctly on the first compilation. If any combination of routing and logic surpass the clock period, the compilation will fail. There are more ways to route a complex algorithm than are possible to compute, so best estimates are made. With a 3D architecture, this issue continues to improve since closer routes would be easier to find in 3D versus 2D. In most cases, written algorithms can simply be recompiled on new architecture (filters and IP processing blocks may need to be reconfigured). Whether GPU computing is used for processing or not, for real-

time display of 3D volumes or large cross sections, it will be needed for high-quality images. Recently, custom implementation of GPU data after processing has been configured as a texture and directly displayed using graphics libraries, such as OpenGL with a GPU application programming interface, such as compute unified device architecture (CUDA) [108, 109]. At the moment, accomplishing real-time volume imaging at video rates for OCT with commercial solutions does not exist and implementing this feature to execute at high speeds is not trivial. Custom software across several different vendors will be needed to accomplish this.

With the ability to visualize the 3D structure and geometry of the BZ, optical mapping [110] makes possible the high resolution recording of function. By using fast voltage-sensitive dyes or calcium indicators with a high resolution camera, the electrical activity of the heart can be mapped during activation. The heart needs to be exposed and well controlled for these experiments, typically with a Langendorff-perfused heart preparation. In Langendorff-perfused hearts, an isolated heart, removed from the animal, is perfused through the aorta with a nourishing solution. These experiments can help model and understand the conditions in which electrical abnormalities resulting from an infarct can lead to electrical complications, such as defibrillation [111]. How electrical activity is altered after an infarct [112] combined with studying the BZ geometry with OCT could tease out pathological indicators in electrical activity to identify candidates for post-infarct arrhythmias.

To more directly measure the BZ, implementing a surface reconstruction algorithm [113, 114] would aid in visualization and investigation of its geometry in relation to electrical abnormalities. Algorithms that accomplish this are quite complex but they are mature, which would simplify implementation. Lastly, using OCT to map coronary vasculature could complement the BZ

structures measured and provide further insights to the relation between coronary vasculature and re-entry [115].

With the cheap cost of CMOS technology, a prototype for a differential camera could be developed to provide an analog balanced detection OCT system. This would then allow for fast enough A-Line rates to be used for functional imaging. To increase stability, non-mechanical scanning for OCT [116] capable of the range required for functional retinal studies could be proposed for high-speed functional imaging. With no mechanical scanning, the stability of the depth profile and repeatability of scans would increase, in turn increasing SNR for cross sectional and volume scanning. An alternative to standard galvo scanning is resonance scanning, which scans in a sinusoidal pattern. The disadvantage of this method is that a correction would be required to linearize the scan. The mostly linear section of the sinusoid pattern can be used as well but then all data on the boundaries would need to be discarded, reducing voxel size and either method would reduce image quality since the galvo is always moving and spends a different amount of time at each A-Line location.

To further increase stability, since the retina is only ~250 μm thick, tighter confocal gating with optical coherence microscopy (OCM) could be utilized to focus on a single layer to measure IOS. The sample optics could be chosen such that the confocal gating of the sample objective is equal to the thickness of the layer to be imaged. One advantage to configuring the sample optics in this fashion would be in the auto-interference terms. Typically the location of surfaces that are producing the auto-interference image are numerous and their origin in the actual image is unknown. With OCM, the possible surface producing auto-interference signals are limited to the layer that is being imaged and therefore would exist only in that layer. Furthermore, adding BD

OCT with OCM and adding the spectra that are out-of-phase instead of subtracting them would result in a signal where the auto-interference terms are doubled. Using the auto-interference terms as a signal would also have less noise since interfering fields would have identical optical paths to and from the sample. Any environmental conditions or imperfect optical elements that would contribute to differences between sample and reference arm that add to the noise level, would not have an effect.

Incorporating adaptive optics [117, 118] would be useful when recording from in-vivo samples to resolve finer detail, compensate for the optical wave front distortions of the cornea, lens and vitreous and aiding in motion artifact removal. Also, Expanding functional imaging into a mammalian model might also produce more prominent, repeatable measurements. The time course for amphibian retinas is 10 times slower than mammals [119] that could make observing fast IOS more likely.

REFERENCES

1. T. Akkin, D. Dave, T. Milner, and H. Rylander Iii, "Detection of neural activity using phase-sensitive optical low-coherence reflectometry," Opt Express **12**, 2377-2386 (2004).
2. K. Bizheva, R. Pflug, B. Hermann, B. Povazay, H. Sattmann, P. Qiu, E. Anger, H. Reitsamer, S. Popov, J. R. Taylor, A. Unterhuber, P. Ahnelt, and W. Drexler, "Optophysiology: depth-resolved probing of retinal physiology with functional ultrahigh-resolution optical coherence tomography," Proc Natl Acad Sci U S A **103**, 5066-5071 (2006).
3. A. A. Moayed, S. Hariri, V. Choh, and K. Bizheva, "In vivo imaging of intrinsic optical signals in chicken retina with functional optical coherence tomography," Opt Lett **36**, 4575-4577 (2011).
4. V. J. Srinivasan, Y. Chen, J. S. Duker, and J. G. Fujimoto, "In vivo functional imaging of intrinsic scattering changes in the human retina with high-speed ultrahigh resolution OCT," Opt Express **17**, 3861-3877 (2009).
5. W. Suzuki, K. Tsunoda, G. Hanazono, and M. Tanifuji, "Stimulus-induced changes of reflectivity detected by optical coherence tomography in macaque retina," Invest Ophthalmol Vis Sci **54**, 6345-6354 (2013).
6. X. C. Yao, A. Yamauchi, B. Perry, and J. S. George, "Rapid optical coherence tomography and recording functional scattering changes from activated frog retina," Appl Opt **44**, 2019-2023 (2005).
7. C. Dunsby and P. French, "Techniques for depth-resolved imaging through turbid media including coherence-gated imaging," Journal of Physics D: Applied Physics **36**, R207 (2003).
8. J. G. Fujimoto, M. E. Brezinski, G. J. Tearney, S. A. Boppart, B. Bouma, M. R. Hee, J. F. Southern, and E. A. Swanson, "Optical biopsy and imaging using optical coherence tomography," Nature Medicine **1**, 970-972 (1995).
9. M. E. Brezinski, G. J. Tearney, B. E. Bouma, J. A. Izatt, M. R. Hee, E. A. Swanson, J. F. Southern, and J. G. Fujimoto, "Optical coherence tomography for optical biopsy properties and demonstration of vascular pathology," Circulation **93**, 1206-1213 (1996).
10. G. J. Tearney, M. E. Brezinski, B. E. Bouma, S. A. Boppart, C. Pitris, J. F. Southern, and J. G. Fujimoto, "In vivo endoscopic optical biopsy with optical coherence tomography," Science **276**, 2037-2039 (1997).
11. D. Huang, E. A. Swanson, C. P. Lin, J. S. Schuman, W. G. Stinson, W. Chang, M. R. Hee, T. Flotte, K. Gregory, C. A. Puliafito, and J. G. Fujimoto, "OPTICAL COHERENCE TOMOGRAPHY," Science **254**, 1178-1181 (1991).

12. J. F. de Boer, B. Cense, B. H. Park, M. C. Pierce, G. J. Tearney, and B. E. Bouma, "Improved signal-to-noise ratio in spectral-domain compared with time-domain optical coherence tomography," Opt Lett **28**, 2067-2069 (2003).
13. W. V. Sorin and D. M. Baney, "A simple intensity noise reduction technique for optical low-coherence reflectometry," Photonics Technology Letters, IEEE **4**, 1404-1406 (1992).
14. S. Yun, G. Tearney, B. Bouma, B. Park, and J. de Boer, "High-speed spectral-domain optical coherence tomography at 1.3 mum wavelength," Opt Express **11**, 3598-3604 (2003).
15. M. Choma, M. Sarunic, C. Yang, and J. Izatt, "Sensitivity advantage of swept source and Fourier domain optical coherence tomography," Opt Express **11**, 2183-2189 (2003).
16. R. Leitgeb, C. Hitzenberger, and A. Fercher, "Performance of fourier domain vs. time domain optical coherence tomography," Opt Express **11**, 889-894 (2003).
17. C. Hitzenberger, E. Goetzinger, M. Sticker, M. Pircher, and A. Fercher, "Measurement and imaging of birefringence and optic axis orientation by phase resolved polarization sensitive optical coherence tomography," Opt Express **9**, 780-790 (2001).
18. A. F. Fercher, C. K. Hitzenberger, G. Kamp, and S. Y. Elzaiat, "Measurement of Intraocular Distances by Backscattering Spectral Interferometry," Optics Communications **117**, 43-48 (1995).
19. A. M. Rollins, R. Ung-Arunyawee, A. Chak, R. C. Wong, K. Kobayashi, M. V. Sivak Jr, and J. A. Izatt, "Real-time in vivo imaging of human gastrointestinal ultrastructure by use of endoscopic optical coherence tomography with a novel efficient interferometer design," Optics Letters **24**, 1358-1360 (1999).
20. S. Radhakrishnan, A. M. Rollins, J. E. Roth, S. Yazdanfar, V. Westphal, D. S. Bardenstein, and J. A. Izatt, "Real-time optical coherence tomography of the anterior segment at 1310 nm," Archives of Ophthalmology **119**, 1179-1185 (2001).
21. A. W. Schaefer, J. J. Reynolds, D. L. Marks, and S. A. Boppart, "Real-time digital signal processing-based optical coherence tomography and Doppler optical coherence tomography," IEEE Trans Biomed Eng **51**, 186-190 (2004).
22. M. W. Jenkins, O. Q. Chughtai, A. N. Basavanhally, M. Watanabe, and A. M. Rollins, "In vivo gated 4D imaging of the embryonic heart using optical coherence tomography," Journal of Biomedical optics **12**, 030505-030505-030503 (2007).
23. T. E. Ustun, N. V. Iftimia, R. D. Ferguson, and D. X. Hammer, "Real-time processing for Fourier domain optical coherence tomography using a field programmable gate array," Review of Scientific Instruments **79**, 114301 (2008).

24. A. E. Desjardins, B. J. Vakoc, M. J. Suter, S. H. Yun, G. J. Tearney, and B. E. Bouma, "Real-time FPGA processing for high-speed optical frequency domain imaging," IEEE transactions on medical imaging **28**, 1468-1472 (2009).
25. G. Liu, J. Zhang, L. Yu, T. Xie, and Z. Chen, "Real-time polarization-sensitive optical coherence tomography data processing with parallel computing," Appl Opt **48**, 6365-6370 (2009).
26. L. An, P. Li, T. T. Shen, and R. Wang, "High speed spectral domain optical coherence tomography for retinal imaging at 500,000 A-lines per second," Biomedical optics express **2**, 2770-2783 (2011).
27. B. Potsaid, I. Gorczynska, V. J. Srinivasan, Y. Chen, J. Jiang, A. Cable, and J. G. Fujimoto, "Ultrahigh speed spectral/Fourier domain OCT ophthalmic imaging at 70,000 to 312,500 axial scans per second," Optics Express **16**, 15149-15169 (2008).
28. W. Wieser, B. R. Biedermann, T. Klein, C. M. Eigenwillig, and R. Huber, "Multi-megahertz OCT: High quality 3D imaging at 20 million A-scans and 4.5 GVoxels per second," Optics Express **18**, 14685-14704 (2010).
29. C. M. Eigenwillig, B. R. Biedermann, G. Palte, and R. Huber, "K-space linear Fourier domain mode locked laser and applications for optical coherence tomography," Optics Express **16**, 8916-8937 (2008).
30. V. M. Gelikonov, G. V. Gelikonov, and P. A. Shilyagin, "Linear-wavenumber spectrometer for high-speed spectral-domain optical coherence tomography," Opt. Spectrosc. **106**, 459-465 (2009).
31. J. Xi, L. Huo, J. Li, and X. Li, "Generic real-time uniform K-space sampling method for high-speed swept-Source optical coherence tomography," Optics Express **18**, 9511-9517 (2010).
32. T. Wu, Z. Ding, L. Wang, and M. Chen, "Spectral phase based k-domain interpolation for uniform sampling in swept-source optical coherence tomography," Optics Express **19**, 18430-18439 (2011).
33. A. Bossen, S. Remund, D. Ernst, C. Meier, T. von Niederhäusern, M. Duelk, and K. Vemishetty, "FPGA-based non-uniform fast Fourier transform (NUFFT) algorithm for real-time OCT signal processing," in *SPIE BiOS*, (International Society for Optics and Photonics, 2013), 85712Y-85712Y-85717.
34. A. A. Claeson, Y.-J. Yeh, A. J. Black, T. Akkin, and V. H. Barocas, "Marker-Free Tracking of Facet Capsule Motion Using Polarization-Sensitive Optical Coherence Tomography," Annals of biomedical engineering, 1-14 (2015).
35. K. K. H. Chan and S. Tang, "High-speed spectral domain optical coherence tomography using non-uniform fast Fourier transform," Biomedical optics express **1**, 1309-1319 (2010).
36. J. Ke, R. Zhu, and E. Y. Lam, "Image reconstruction from nonuniformly spaced samples in Fourier domain optical coherence tomography," in *IS&T/SPIE*

Electronic Imaging, (International Society for Optics and Photonics, 2012), 829610-829610-829618.
37. M. Sylwestrzak, M. Szkulmowski, D. Szlag, and P. Targowski, "Real-time imaging for spectral optical coherence tomography with massively parallel data processing," Photonics Letters of Poland **2**, pp. 137-139 (2010).
38. J. Li, M. V. Sarunic, and L. Shannon, "Scalable, High Performance Fourier Domain Optical Coherence Tomography: Why FPGAs and Not GPGPUs," in *Field-Programmable Custom Computing Machines (FCCM), 2011 IEEE 19th Annual International Symposium on*, (IEEE, 2011), 49-56.
39. L. Shannon, J. Li, M. R. Mohammadnia, and M. V. Sarunic, "Evaluating the scalability of high-performance, Fourier-Domain Optical Coherence Tomography on GPGPUs and FPGAs," in *Signals, Systems and Computers (ASILOMAR), 2011 Conference Record of the Forty Fifth Asilomar Conference on*, (IEEE, 2011), 483-487.
40. B. E. Applegate, J. Park, E. Carbajal, D. Schmidt, and K. Vemishetty, "Quantitative comparison of hardware architectures for high-speed processing in optical coherence tomography," in *SPIE BiOS*, (International Society for Optics and Photonics, 2012), 821332-821332-821336.
41. D. Xu, Y. Huang, and J. U. Kang, "Real-time compressive sensing spectral domain optical coherence tomography," Optics Letters **39**, 76-79 (2014).
42. L. Thrane, H. E. Larsen, K. Norozi, F. Pedersen, J. B. Thomsen, M. Trojer, and T. M. Yelbuz, "Field programmable gate-array-based real-time optical Doppler tomography system for in vivo imaging of cardiac dynamics in the chick embryo," Optical Engineering **48**, 023201-023201-023213 (2009).
43. Y. Pan and D. L. Farkas, "Noninvasive imaging of living human skin with dual-wavelength optical coherence tomography in two and three dimensions," Journal of Biomedical optics **3**, 446-455 (1998).
44. F. Spöler, S. Kray, P. Grychtol, B. Hermes, J. Bornemann, M. Först, and H. Kurz, "Simultaneous dual-band ultra-high resolution optical coherence tomography," Optics Express **15**, 10832-10841 (2007).
45. Y.-J. Yeh, A. J. Black, and T. Akkin, "Spectral-domain low-coherence interferometry for phase-sensitive measurement of Faraday rotation at multiple depths," Applied Optics **52**, 7165-7170 (2013).
46. S. Shin, U. Sharma, H. Tu, W. Jung, and S. A. Boppart, "Characterization and analysis of relative intensity noise in broadband optical sources for optical coherence tomography," Photonics Technology Letters, IEEE **22**, 1057-1059 (2010).
47. A. G. Podoleanu, "Unbalanced versus balanced operation in an optical coherence tomography system," Applied Optics **39**, 173-182 (2000).

48. R. Leitgeb, W. Drexler, A. Unterhuber, B. Hermann, T. Bajraszewski, T. Le, A. Stingl, and A. Fercher, "Ultrahigh resolution Fourier domain optical coherence tomography," Optics Express **12**, 2156-2165 (2004).
49. R. A. Leitgeb, C. K. Hitzenberger, A. F. Fercher, and T. Bajraszewski, "Phase-shifting algorithm to achieve high-speed long-depth-range probing by frequency-domain optical coherence tomography," Optics Letters **28**, 2201-2203 (2003).
50. J. Zhang, J. S. Nelson, and Z. P. Chen, "Removal of a mirror image and enhancement of the signal-to-noise ratio in Fourier-domain optical coherence tomography using an electro-optic phase modulator," Optics Letters **30**, 147-149 (2005).
51. M. Wojtkowski, A. Kowalczyk, R. Leitgeb, and A. F. Fercher, "Full range complex spectral optical coherence tomography technique in eye imaging," Opt Lett **27**, 1415-1417 (2002).
52. B. Bouma, M. Brezinski, J. Fujimoto, G. Tearney, S. Boppart, and M. Hee, "High-resolution optical coherence tomographic imaging using a mode-locked Ti: Al 2 O 3 laser source," Optics Letters **20**, 1486-1488 (1995).
53. A. Bradu and A. G. Podoleanu, "Fourier domain optical coherence tomography system with balance detection," Optics Express **20**, 17522-17538 (2012).
54. W. C. Kuo, C. M. Lai, Y. S. Huang, C. Y. Chang, and Y. M. Kuo, "Balanced detection for spectral domain optical coherence tomography," Opt Express **21**, 19280-19291 (2013).
55. J. Ai and L. V. Wang, "Synchronous self-elimination of autocorrelation interference in Fourier-domain optical coherence tomography," Optics Letters **30**, 2939-2941 (2005).
56. W. C. Kuo, Y. S. Lai, C. M. Lai, and Y. S. Huang, "Balanced detection spectral domain optical coherence tomography with a multiline single camera for signal-to-noise ratio enhancement," Appl Opt **51**, 5936-5940 (2012).
57. J. F. de Boer, T. E. Milner, M. J. van Gemert, and J. S. Nelson, "Two-dimensional birefringence imaging in biological tissue by polarization-sensitive optical coherence tomography," Opt Lett **22**, 934-936 (1997).
58. H. Wang, M. K. Al-Qaisi, and T. Akkin, "Polarization-maintaining fiber based polarization-sensitive optical coherence tomography in spectral domain," Optics Letters **35**, 154-156 (2010).
59. V. V. Tuchin, X. Xu, and R. K. Wang, "Dynamic optical coherence tomography in studies of optical clearing, sedimentation, and aggregation of immersed blood," Applied Optics **41**, 258-271 (2002).
60. R. K. Wang, X. Xu, V. V. Tuchin, and J. B. Elder, "Concurrent enhancement of imaging depth and contrast for optical coherence tomography by hyperosmotic agents," JOSA B **18**, 948-953 (2001).
61. H. Ashikaga, S. R. Mickelsen, D. B. Ennis, I. Rodriguez, P. Kellman, H. Wen, and E. R. McVeigh, "Electromechanical analysis of infarct border zone in chronic

myocardial infarction," American Journal of Physiology-Heart and Circulatory Physiology **289**, H1099-H1105 (2005).
62. P. C. Ursell, P. I. Gardner, A. Albala, J. Fenoglio, and A. L. Wit, "Structural and electrophysiological changes in the epicardial border zone of canine myocardial infarcts during infarct healing," Circulation Research **56**, 436-451 (1985).
63. D. J. Hearse and D. M. Yellon, "The "border zone" in evolving myocardial infarction: controversy or confusion?," The American journal of cardiology **47**, 1321-1334 (1981).
64. D. M. Yellon, D. J. Hearse, R. Crome, J. Grannell, and R. K. Wyse, "Characterization of the lateral interface between normal and ischemic tissue in the canine heart during evolving myocardial infarction," The American journal of cardiology **47**, 1233-1239 (1981).
65. R. Axford-Gatley and G. Wilson, "The" border zone" in myocardial infarction. An ultrastructural study in the dog using an electron-dense blood flow marker," The American journal of pathology **131**, 452 (1988).
66. B. M. Jackson, J. H. Gorman, I. S. Salgo, S. L. Moainie, T. Plappert, M. S. John-Sutton, L. H. Edmunds, and R. C. Gorman, "Border zone geometry increases wall stress after myocardial infarction: contrast echocardiographic assessment," American Journal of Physiology-Heart and Circulatory Physiology **284**, H475-H479 (2003).
67. A. K. Jeong, S. I. Choi, D. H. Kim, S. B. Park, S. S. Lee, S. H. Choi, and T.-H. Lim, "Evaluation by contrast-enhanced MR imaging of the lateral border zone in reperfused myocardial infarction in a cat model," Korean Journal of Radiology **2**, 21-27 (2001).
68. G. Gottlieb, S. Kubo, and D. Alonso, "Ultrastructural characterization of the border zone surrounding early experimental myocardial infarcts in dogs," The American journal of pathology **103**, 292 (1981).
69. M. J. Janse, F. Van Capelle, H. Morsink, A. G. Kléber, F. Wilms-Schopman, R. Cardinal, C. N. d'Alnoncourt, and D. Durrer, "Flow of" injury" current and patterns of excitation during early ventricular arrhythmias in acute regional myocardial ischemia in isolated porcine and canine hearts. Evidence for two different arrhythmogenic mechanisms," Circulation Research **47**, 151-165 (1980).
70. D. T. Wong, M. J. Weightman, M. Baumert, H. Tayeb, J. D. Richardson, R. Puri, A. G. Bertaso, K. C. Roberts-Thomson, P. Sanders, and M. I. Worthley, "Electro-mechanical characteristics of myocardial infarction border zones and ventricular arrhythmic risk: novel insights from grid-tagged cardiac magnetic resonance imaging," European radiology **22**, 1651-1658 (2012).
71. A. T. Yan, A. J. Shayne, K. A. Brown, S. N. Gupta, C. W. Chan, T. M. Luu, M. F. Di Carli, H. G. Reynolds, W. G. Stevenson, and R. Y. Kwong, "Characterization of the peri-infarct zone by contrast-enhanced cardiac magnetic resonance imaging

is a powerful predictor of post–myocardial infarction mortality," Circulation **114**, 32-39 (2006).
72. S. Factor, E. Sonnenblick, and E. Kirk, "The histologic border zone of acute myocardial infarction--islands or peninsulas?," The American journal of pathology **92**, 111 (1978).
73. R. M. Smith, A. Matiukas, C. W. Zemlin, and A. M. Pertsov, "Nondestructive optical determination of fiber organization in intact myocardial wall," Microscopy Research and Technique **71**, 510-516 (2008).
74. X. Xu and R. K. Wang, "The role of water desorption on optical clearing of biotissue: studied with near infrared reflectance spectroscopy," Medical physics **30**, 1246-1253 (2003).
75. R. M. Smith, A. J. Black, S. S. Velamakanni, T. Akkin, and E. G. Tolkacheva, "Visualizing the complex 3D geometry of the perfusion border zone in isolated rabbit heart," Applied Optics **51**, 2713-2721 (2012).
76. M. K. Al-Qaisi and T. Akkin, "Polarization-sensitive optical coherence tomography based on polarization-maintaining fibers and frequency multiplexing," Opt Express **16**, 13032-13041 (2008).
77. H. Peng, Z. Ruan, F. Long, J. H. Simpson, and E. W. Myers, "V3D enables real-time 3D visualization and quantitative analysis of large-scale biological image data sets," Nature biotechnology **28**, 348-353 (2010).
78. C. P. Fleming, C. M. Ripplinger, B. Webb, I. R. Efimov, and A. M. Rollins, "Quantification of cardiac fiber orientation using optical coherence tomography," Journal of Biomedical optics **13**, 030505-030505-030503 (2008).
79. J. M. Enoch, F. L. Tobey, and H. E. Bedell, *Vertebrate photoreceptor optics* (Springer-Verlag, 1981).
80. J. M. Enoch, "Vertebrate receptor optics and orientation," Documenta Ophthalmologica **48**, 373-388 (1980).
81. M. Hammer, A. Roggan, D. Schweitzer, and G. Muller, "Optical properties of ocular fundus tissues-an in vitro study using the double-integrating-sphere technique and inverse Monte Carlo simulation," Physics in Medicine and Biology **40**, 963 (1995).
82. L. Rovati, S. Cattini, N. Zambelli, F. Viola, and G. Staurenghi, "In-vivo diffusing-wave-spectroscopy measurements of the ocular fundus," Optics Express **15**, 4030-4038 (2007).
83. K. Hofmann, R. Uhl, W. Hoffmann, and W. Kreutz, "Measurements of fast light-induced light-scattering and-absorption changes in outer segments of vertebrate light sensitive rod cells," Biophysics of structure and mechanism **2**, 61-77 (1976).
84. H. Harary, J. Brown, and L. Pinto, "Rapid light-induced changes in near infrared transmission of rods in Bufo marinus," Science **202**, 1083-1085 (1978).
85. H. Kühn, N. Bennett, M. Michel-Villaz, and M. Chabre, "Interactions between photoexcited rhodopsin and GTP-binding protein: kinetic and stoichiometric

analyses from light-scattering changes," Proceedings of the National Academy of Sciences **78**, 6873 (1981).
86. M. Heck, A. Pulvermüller, and K. P. Hofmann, "[22] Light scattering methods to monitor interactions between rhodopsin-containing membranes and soluble proteins," Methods in enzymology **315**, 329-347 (2000).
87. E. Pugh and T. Lamb, "Cyclic GMP and calcium: the internal messengers of excitation and adaptation in vertebrate photoreceptors," Vision research **30**, 1923-1948 (1990).
88. D. R. Pepperberg, M. Kahlert, A. Krause, and K. P. Hofmann, "Photic modulation of a highly sensitive, near-infrared light-scattering signal recorded from intact retinal photoreceptors," Proceedings of the National Academy of Sciences **85**, 5531-5535 (1988).
89. V. Y. Arshavsky, T. D. Lamb, and E. N. Pugh, Jr., "G proteins and phototransduction," Annu Rev Physiol **64**, 153-187 (2002).
90. R. A. Weale, "On the birefringence of rods and cones," Pflugers Arch. **329**, 244-257 (1971).
91. J. M. Enoch, J. Scandrett, and F. L. Tobey, "A study of the effects of bleaching on the width and index of refraction of frog rod outer segments," Vision research **13**, 171-IN173 (1973).
92. R. Lu, A. M. Levy, Q. Zhang, S. J. Pittler, and X. Yao, "Dynamic near-infrared imaging reveals transient phototropic change in retinal rod photoreceptors," Journal of Biomedical optics **18**, 106013-106013 (2013).
93. M. P. Gray-Keller and P. B. Detwiler, "The calcium feedback signal in the phototransduction cascade of vertebrate rods," Neuron **13**, 849-861 (1994).
94. G. Hanazono, K. Tsunoda, K. Inomata, Y. Kazato, and M. Tanifuji, "Flash-Evoked Light Reflectance Changes of the Optic Disk Reflect the Neural Activity of the Inner Retina," Investigative ophthalmology & visual science **48**, 528-528 (2007).
95. L. B. Cohen, R. D. Keynes, and B. Hille, "Light scattering and birefringence changes during nerve activity," Nature **218**, 438-441 (1968).
96. A. J. Foust and D. M. Rector, "Optically teasing apart neural swelling and depolarization," Neuroscience **145**, 887-899 (2007).
97. R. D. Andrew and B. A. MacVicar, "Imaging cell volume changes and neuronal excitation in the hippocampal slice," Neuroscience **62**, 371-383 (1994).
98. K. Holthoff and O. W. Witte, "Intrinsic optical signals in rat neocortical slices measured with near-infrared dark-field microscopy reveal changes in extracellular space," J Neurosci **16**, 2740-2749 (1996).
99. R. A. Stepnoski, A. LaPorta, F. Raccuia-Behling, G. E. Blonder, R. E. Slusher, and D. Kleinfeld, "Noninvasive detection of changes in membrane potential in cultured neurons by light scattering," Proc Natl Acad Sci U S A **88**, 9382-9386 (1991).

100. I. Tasaki and P. M. Byrne, "Rapid structural changes in nerve fibers evoked by electric current pulses," Biochem Biophys Res Commun **188**, 559-564 (1992).
101. T. Akkin, D. Landowne, and A. Sivaprakasam, "Detection of neural action potentials using optical coherence tomography: intensity and phase measurements with and without dyes," Frontiers in Neuroenergetics (2010).
102. I. Tasaki and T. Nakaye, "Rapid mechanical responses of the dark-adapted squid retina to light pulses," Science **223**, 411-413 (1984).
103. X. C. Yao and J. S. George, "Dynamic neuroimaging of retinal light responses using fast intrinsic optical signals," Neuroimage **33**, 898-906 (2006).
104. X. C. Yao and Y. B. Zhao, "Optical dissection of stimulus-evoked retinal activation," Opt Express **16**, 12446-12459 (2008).
105. B. Wang, R. Lu, Q. Zhang, Y. Jiang, and X. Yao, "En face optical coherence tomography of transient light response at photoreceptor outer segments in living frog eyecup," Optics Letters **38**, 4526-4529 (2013).
106. E. R. Stevens, E. C. Gustafson, and R. F. Miller, "Glycine transport accounts for the differential role of glycine vs. d-serine at NMDA receptor coagonist sites in the salamander retina," European Journal of Neuroscience **31**, 808-816 (2010).
107. V. J. Srinivasan, D. C. Adler, Y. Chen, I. Gorczynska, R. Huber, J. S. Duker, J. S. Schuman, and J. G. Fujimoto, "Ultrahigh-speed optical coherence tomography for three-dimensional and en face imaging of the retina and optic nerve head," Investigative ophthalmology & visual science **49**, 5103 (2008).
108. Y. Jian, K. Wong, and M. V. Sarunic, "Graphics processing unit accelerated optical coherence tomography processing at megahertz axial scan rate and high resolution video rate volumetric rendering," Journal of Biomedical optics **18**, 026002-026002 (2013).
109. W. Wieser, W. Draxinger, T. Klein, S. Karpf, T. Pfeiffer, and R. Huber, "High definition live 3D-OCT in vivo: design and evaluation of a 4D OCT engine with 1 GVoxel/s," Biomedical optics express **5**, 2963-2977 (2014).
110. I. R. Efimov, V. P. Nikolski, and G. Salama, "Optical imaging of the heart," Circulation Research **95**, 21-33 (2004).
111. K. Nanthakumar, J. Jalife, S. Massé, E. Downar, M. Pop, J. Asta, H. Ross, V. Rao, S. Mironov, and E. Sevaptsidis, "Optical mapping of Langendorff-perfused human hearts: establishing a model for the study of ventricular fibrillation in humans," American Journal of Physiology-Heart and Circulatory Physiology **293**, H875-H880 (2007).
112. W. R. Mills, N. Mal, F. Forudi, Z. B. Popovic, M. S. Penn, and K. R. Laurita, "Optical mapping of late myocardial infarction in rats," American Journal of Physiology-Heart and Circulatory Physiology **290**, H1298-H1306 (2006).
113. W. E. Lorensen and H. E. Cline, "Marching cubes: A high resolution 3D surface construction algorithm," in *ACM siggraph computer graphics*, (ACM, 1987), 163-169.

114. H. Hoppe, T. DeRose, T. Duchamp, J. McDonald, and W. Stuetzle, *Surface reconstruction from unorganized points* (ACM, 1992), Vol. 26.
115. M. J. Bishop, G. Plank, and E. Vigmond, "Investigating the role of the coronary vasculature in the mechanisms of defibrillation," Circulation: Arrhythmia and Electrophysiology **5**, 210-219 (2012).
116. Y. Watanabe, K. Yamada, and M. Sato, "In vivo non-mechanical scanning grating-generated optical coherence tomography using an InGaAs digital camera," Optics Communications **261**, 376-380 (2006).
117. R. J. Zawadzki, S. M. Jones, S. S. Olivier, M. Zhao, B. A. Bower, J. A. Izatt, S. Choi, S. Laut, and J. S. Werner, "Adaptive-optics optical coherence tomography for high-resolution and high-speed 3D retinal in vivo imaging," Opt Express **13**, 8532-8546 (2005).
118. Y. Zhang, J. Rha, R. Jonnal, and D. Miller, "Adaptive optics parallel spectral domain optical coherence tomography for imaging the living retina," Opt Express **13**, 4792-4811 (2005).
119. E. Pugh Jr and T. Lamb, "Amplification and kinetics of the activation steps in phototransduction," Biochimica et Biophysica Acta **1141**, 111 (1993).